Microstructure and Oxidation Behavior Comparison Between Vertical, Upskin and Unsupported Downskin Structures of SS316L made with Laser Powder Bed Fusion

Omar R. Binfahad

Masters of Science in Mining and Materials Engineering

School of Mining and Materials Engineering

McGill University

Montreal, Quebec, Canada

September 14, 2024

A thesis submitted to McGill University in partial fulfillment of the requirements of the degree of Masters of Science in Mining and Materials Engineering

Abstract

As the laser powder bed fusion (LPBF) technology progresses, developing protocols for reducing and/or supportless printing of overhang downward-facing surfaces becomes increasingly critical for enhancing the economic and environmental efficiency of the process. The present study investigates the possible mismatch in microstructural, mechanical and oxidation behaviour of LPBF SS316L samples printed at 90 and 0° angles and including downward-facing low-angle overhang surfaces, in both as-built and heat-treated conditions. In as-built (AB) condition, primary dendrite arm spacing (PDAS) was measured at 0.72 ± 0.09 and 3.19 ± 0.20 µm for the bulk and downskin surface, yielding a microhardness value of 244 ± 5 and 225 ± 3 HV, respectively. In addition, secondary dendritic arms are observed to form at the downskin, where the secondary dendrite arm spacing (SDAS) is measured at 0.99 ± 0.18 µm. A continuous growth model microsegregation analysis showed microsegregation level near equilibrium values. For the heat treated (HT) condition, the cellular structure recrystallized, leading to a grain size measurement of 31 ± 3 and 26 ± 3 µm at the bulk and downskin surfaces, respectively, revealing that the grain growth rate observed at the downskin surfaces is slower than that of the bulk. The microhardness values were measured at 184 ± 4 and 195 ± 3 HV for the HT bulk and downskin surfaces. Post 100 hrs. of oxidation treatment at 900°C, x-ray diffraction (XRD) analysis confirmed the formation of Fe_2O_3, Cr_2O_3, Cr_2FeO_4 and Cr_2MnO_4 oxides at the AB and HT bulk and downskin surfaces. While the scale thickness for the bulk and downskin were measured at 3.7 ± 1.7, 3.8 ± 1.8 and 7.9 ± 2.4 and 7.1 ± 2.1 µm for the AB and HT condition, respectively. Electron dispersive spectroscopy (EDS) analysis revealed the formation of SiO_2 oxide along the grain boundaries.

Résumé

Au fur et à mesure que la technologie LPBF progresse, le développement de protocoles pour l'impression réduite et/ou sans support de surfaces en porte-à-faux orientées vers le bas devient de plus en plus essentiel pour améliorer l'efficacité économique et environnementale du processus. Par conséquent, cette thèse pose un contexte fondamental de la procédure, des paramètres, des propriétés résultantes et de sa performance économique globale. Avec un manque de connaissances dans la littérature disponible, cette recherche cherche à apporter de nouvelles idées et de nouveaux résultats pour développer et explorer davantage ladite technologie. La présente étude examine le décalage possible dans le comportement microstructurel, mécanique et à l'oxydation des échantillons LPBF SS316L imprimés à des angles de 90 et 0° et y compris les surfaces en porte-à-faux à faible angle orientées vers le bas, à la fois dans des conditions telles que construites et traitées thermiquement. Dans des conditions AB, le PDAS a été mesuré à 0,72 ± 0,09 et 3,19 ± 0,20 μm pour la surface en vrac et la surface duvet, ce qui a donné une valeur de microdureté de 244 ± 5 et 225 ± 3 HV, respectivement. De plus, on observe la formation de bras dendritiques secondaires au niveau de la peau duveteuse, où le SDAS est mesuré à 0,99 ± 0,18 μm. Une analyse de microségrégation sur modèle de croissance continue a montré un niveau de microségrégation proche des valeurs d'équilibre. Pour la condition HT, on observe que la structure cellulaire se recristallise, ce qui conduit à une mesure de la taille des grains de 31 ± 3 et de 26 ± 3 μm aux surfaces de la peau en vrac et de la peau duveteuse, respectivement, révélant que le taux de recristallisation observé aux surfaces de la peau inférieure est plus lent que celui de la peau en vrac. Les valeurs de microdureté ont été mesurées à 184 ± 4 et 195 ± 3 HV sur les surfaces HT en vrac et en duvet. Poste 100 hrs. traitement oxydatif à 900°C, l'analyse XRD a confirmé la

formation d'oxydes Fe2O3, Cr2O3, Cr2FeO4 et Cr2MnO4 sur les surfaces en vrac et en duvet AB et HT. Alors que l'épaisseur de l'échelle pour le vrac et le duvet est mesurée à 3,7 ± 1,7, 3,8 ± 1,8 et 7,9 ± 2,4 et 7,1 ± 2,1 µm pour les conditions AB et HT, respectivement. L'analyse EDS a révélé la formation d'oxyde de SiO2 le long des joints de grains. Ces informations permettent de poursuivre les développements vers une commercialisation réussie de la fabrication sans support LPBF.

Acknowledgments

The completion of this thesis marks a significant milestone, one that would not have been possible without the support and guidance of many individuals.

I would like to thank my supervisor Dr. Mathieu Brochu for giving me the opportunity to pursue this research. Your mentorship and teaching have been instrumental in my studies, and has allowed me to grow as a scientist and an engineer. I hope that I can repay a tiny fraction with attempts at Arabic lessons.

I would like to acknowledge, thank and show my sincere appreciation to the presidential courts in Abu Dhabi (UAE) for the trust and support given to me throughout my studies.

I would also like to recognize and thank my friends and colleagues from the Powder Processing and Additive Manufacturing of Advanced Materials (P^2 $[AM]^2$) research group. This work is a product of extensive collaboration, and would have been impossible without your support. Many thanks go to An, Anne, Anubhav, Corina, Emilio, Guohong, Ivonne, Jaskaranpal, Mahmoud, Mohammad, Mohamad (Abo Omar), Mohamad (Sayed), Murali, Pablo, Pierre, Qi, Rafeal, Shipei, and Srikanta. I want to give a special mention to Amit, Ashutosh, and Satish who played a fundamental role in my project. To all those I forget to mention, I apologize but please know I'm grateful.

I owe a huge thank you to my family for their support during my time abroad, especially to my parents, who have always encouraged me to pursue my academic goals while being far from home. شكرا

Last but most importantly, I want to thank my wife, Valentina, for her constant support, encouragement, and love throughout this journey. (P.S. A special thank you to Sia & Milo as well.)

Table of Contents

List of figures & Tables

Figures

Tables

List of abbreviations

Abbreviations	Meaning	Abbreviations	Meaning
AM	Additive Manufacturing	***Ar***	Argon
TM	Traditional Manufacturing	***He***	Helium
LPBF	Laser Powder Bed Fusion	***LT***	Layer Thickness
Al	Aluminum	***ED***	Energy Density
Ti	Titanium	***HD***	Hatch Distance
Ni	Nickle	***PSD***	Powder Size Distribution
Cu	Copper	***G***	Thermal Gradient
SS	Stainless Steel	***R***	Solidification Velocity
HV	Microhardness - Vickers	***CR/ε***	Cooling Rate
TS	Tensile Strength	***BD***	Build Direction
Cr	Chromium	***YS***	Yield Strength
AB	As Built	***UTS***	Ultimate Tensile Strength
HT	Heat Treatment/ed	***COD***	Crystallography Open Database
SEM	Scanning Electron Microscope	***PDAS***	Primary Dendritic Arm Spacing
OM	Optical Microscope	***SDAS/λ***	Secondary Dendritic Arm Spacing
EBSD	Electron Backscatter Diffraction	***IPF***	Inverse Pole Figure
XRD	X-ray Diffraction	***PF***	Pole Figure
EDS	Energy Dispersive Spectroscopy	***MUD***	Multiple of Uniform Density
SM	Subtractive Manufacturing	***AR***	Aspect Ratio
CNC	Computer Numerical Control	***DS***	Downskin
CAD	Computer-Aided Design	**λ**	thermal conductivity
STL	Standard Triangulate Language	$\mathbf{T_{boiling}}$	Boiling Temperature
ASTM	American Society for Testing and Materials	$\mathbf{T_{liquidus}}$	Liquidus Temperature
PBF	Powder Bed Fusion	***SFV***	Solidification Front Velocity
EPBF	Electron Beam Powder Bed Fusion	**K(v)**	Partition Coefficient
SLM	Selective Laser Melting	***CET***	Columnar-to-Equiaxed Transition

Chapter 1 Introduction

1.1 Background

AM offers distinct advantages over TM in high-complexity, low-tolerance sectors such as the aerospace [1-3] and medical [4-7] industries. This is a result of the unique ability of the processes to fabricate parts and structures with increased geometric complexity while minimizing waste material [5, 7]. LPBF is a key AM process that has been widely discussed in literature [8, 9]. The LPBF process can be described as an iterative process whereby a laser is used to selectively melt and solidify powder layers until the final component is formed.

The increased popularity of the LPBF process has led to a significant number of studies into the use of a variety of metallic alloys, such as Al [10-12], Ti [13-15], Ni [16-18] and Cu [19-21] alloys. Within all alloy families, SS alloys such as SS316L have generated significant attention due to their compelling mechanical properties and excellent corrosion resistance [22-24]. However, the majority of the published studies have focused on process optimization [25, 26] and the correlation between microstructure and mechanical properties [27, 28].

A review of the literature revealed the superiority of LPBF SS316L mechanical properties over its wrought counterpart due to the unique microstructure [22, 29]. Nonetheless, due to the developed long columnar grains, studies have been conducted to eliminate the anisotropy through post-processing heat treatments [25, 30-32]. The disadvantage of the applied heat treatment is observed in the reduction in hardness (HV) and TS due to the removal of the residual stresses, dissolution of cells, change in grain size and grain boundary density [25, 30-32].

The oxidation resistance of LPBF SS316L is another pillar behind its popularity, due to the alloying Cr allowing for the development of a protective Cr_2O_3 oxide scale at an onset temperature between 400 to 500 °C [33-38]. In addition, LPBF SS316L was shown to have slower oxidation kinetics than the wrought counterpart [22, 39-41].

Support structures are commonly used during LPBF due to improvements in part thermal and geometric stability and limited cost reduction [42]. Studies have shown the high cost involved in the support removal process, nearly 50% at nine parts per build [42]. This presents a window into which the production cost of LPBF parts may be reduced significantly by developing protocols with reduced and supportless printing for overhang downward-facing surfaces.

Initial studies reported the formation of coarser microstructure features at the support-less downward facing overhang surfaces (Downskin) [43-46]. This results in a mismatch in mechanical properties as reported by Kumar et al. [43] and Viale et al. [44].

While the outcomes of achieving excellent supportless printing may be of high interest to the LPBF industry, studies conducted on its effects has been limited to establishing the process parameter to achieve successful supportless printing [44] and the resultant dimensional tolerances and surface properties [45].

1.2 Objectives

Due to the inherent complexity of supportless low angle overhang printing, to date, no data in literature exists to delineate a potential mismatch in oxidation response of supportless LPBF due to the rise in difference in microstructure. Therefore, the present study aims to explore the relationship between the printing angle on AB and HT microstructure and the oxidation behaviour of a LPBF SS316 support-less structure. Particularly, this study has the following objectives:

1. To validate the ability to print supportless LPBF SS316L structure.
2. To characterize the microstructure with relation to the printing angle in AB and HT conditions.
3. To quantify the mechanical properties with relation to the printing angle in AB and HT conditions.
4. To explore the oxidation behaviour with relation to the printing angle in AB and HT conditions.

1.3 Thesis Layout

The main body of this thesis is divided in five different chapters. The current **Chapter 1** is served as an introduction to the background and the main objectives of the present thesis. **Chapter 2** provides an exploration of the available literature, starting with describing AM, LPBF, and the parameters that are involved in the process. Followed by common materials used in LPBF including SS316L and its microstructure, mechanical and oxidative properties. This chapter also reports a cost study on the LPBF process and the current knowledge regarding supportless printing. After displaying the need for supportless printing protocols, **Chapter 3** presents the methodology used to achieve the objectives of this study. This chapter also previews the acquired results. **Chapter 4** serves as a discussion of the results, and a comparison to pre-existing knowledge in literature. Finally, **Chapter 5** presents the summery and conclusions of the study. Here, the author suggests areas for further developments and studies.

Chapter 2 Literature

Traditional Manufacturing (TM), or Subtractive manufacturing (SM), refers to the manufacturing technologies in which martial is removed from its original form (billet or block) to achieve the desired net shape. The main four families of TM are turning, drilling, milling and laser cutting such as Computer Numerical Control (CNC) manufacturing.

Another form of TM processes involves a mold and a metallic alloy in liquid state. Such processes fall under the umbrella of metallic casting, including but not limited to: sand casting, die casting and Injection molding.

The Commonalities between all TM processes is the decrease in volume of starting part during the manufacturing process. Figure 1 presents a schematic of a TM process. Therefore, the clear issue that arises during TM is due to the inherent limitations in the complexity and customization of manufactured parts, coupled with significant waste material generated in the machining process [47].

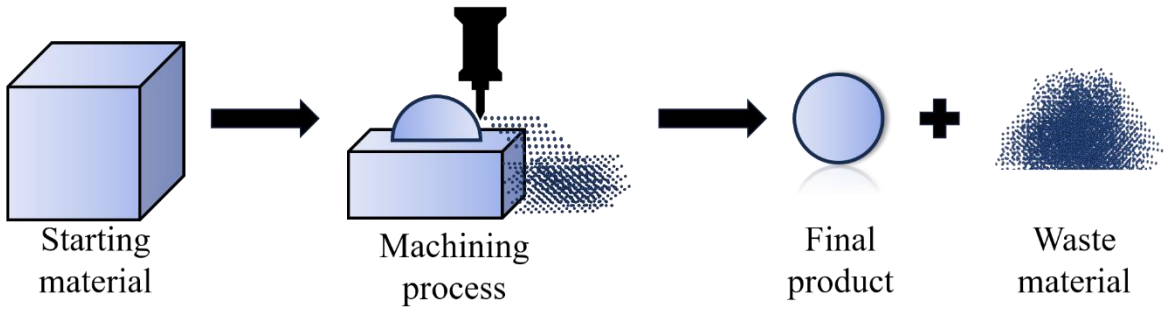

Figure 1. A schematic of Traditional/ Subtractive Manufacturing (TM/SM)

With regards to the limitations involved in TM processes, studies and long history of applications have shown three main areas that create drawbacks[48]:

- **Production of high material waste**

  Due to the nature of the TM processes, the production of a single unit creates large relative volume of waste material.

  In TM, the buy-to-fly ratio is typically used as a metric to measure the waste generated in a manufacturing process. A buy-to-fly ratio is the mass of the starting billet of material to the mass of the finished part. A typical ratio used in the aerospace industry is 10, meaning only 10% of the original starting material remains in the final part after the machining process [49].

- **Ridged boundaries concerning design prototype**

  In addition to the generated waste, the use of premanufactured tools within TM processes creates a limitation to modify the design of prefabricated tool parts. Thus, the is little to no ability to modify a design once a tool to manufactured [48].

- **High cost for low to medium production volume**

  Finally, due to the need of prefabricated tools, the initial expense is high, leading the production cost to decrease as a function of increasing production volume (i.e. decreasing cost-per-part). Therefore, for a TM process to be economically viable, a large volume of production is necessary [47].

In an effort to lower manufacturing cost of metallic parts and expand the manufacturing capabilities, AM was introduced in the 1960s [48]. Ever since, the AM field has gone through several waves of growth, expanding the limits imposed by TM.

2.1 Additive Manufacturing

AM refers to a manufacturing process in which a geometrically complex structure is fabricated in a layer-by-layer form, using a 3D computer-aided-design (CAD) model data [50-52]. Figure 2 presents a schematic of a basic AM process. In comparison to TM, studies have demonstrated that AM significantly improves material efficiency. Specifically, the buy-to-fly ratio was reduced from 30:1 to nearly 3:1 [53].

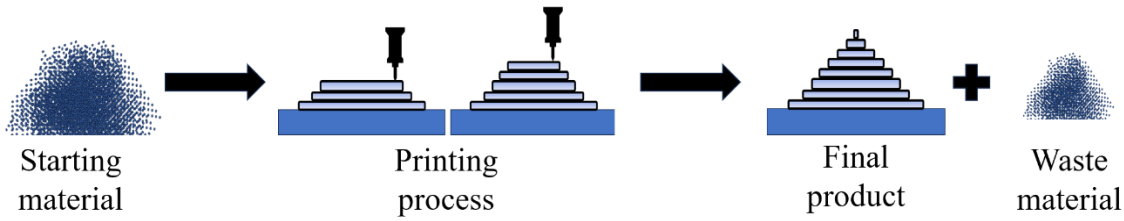

Figure 2. A schematic of Additive Manufacturing (AM)

In addition, Figure 3 presents the basic setup in which the 3D model data is transformed into a final physical part. In summary, the 3D model data is translated into a standard triangulate language (STL) format file, which is imported into an AM printer to dictate the printing process [51].

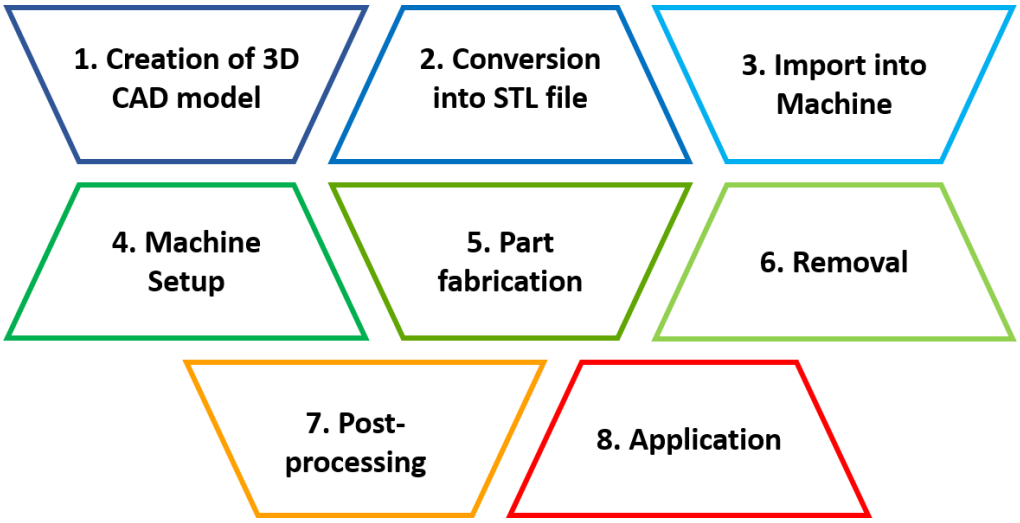

Figure 3. The general steps in AM [50, 51].

The significant positive impact of the different AM processes is observed in several low-tolerance fields. The aerospace field benefits from lighter, intricate and highly optimized components, subsequently impacting the sustainability of the field as a whole [1-3, 54]. For the medical field, AM provides the benefits in the ability to fabricate patient-specific parts, leading to a cost-effective fabrication [4-7]. Overall, the advancements achieved via AM are due to the possibility of fabricating parts with increased complexity while minimizing waste material [5, 7].

The advantages of AM technologies can be summarized through the following four points:

- *Material efficiency*: In the metal AM sector, a reduction of up to 40% of raw material waste compared to TM is achieved due to the layer-by-layer building procedure [55]. In addition to 95-98% of non-melted metal powders can be recycled for future fabrications.

- *Resource efficiency*: Since AM processes do not need any additional resources, parts can be produced by small manufacturers, improving a part of the supply chain [56]. This allows for specialized applications such as jewelry and watch making [57, 58].
- *Design flexibility*: The nature of AM allows for a higher level of design freedom compared to TM. This freedom is not only limited to the geometrical aspect, but to the mechanical properties (i.e. a gradient of properties within a structure) [56].
- *Production flexibility*: Unlike TM, where molds and pre-fabricated tools are necessary, AM allows for the flexibility in applying design changes frequently. This property is advantageous to small/medium and short production volumes/cycles [59]

Under the umbrella of AM, the American society for testing and materials (ASTM) has highlighted seven main categories, namely: material extrusion, material jetting, vat polymerization, sheet lamination, binder jetting, direct energy deposition and powder bed fusion [60-62]. The distinction between the seven categories arises within the form of the starting material (i.e. ceramics, plastics, metal powder or filament), the energy source (i.e. laser, electron beam or plasma arc), and the printing process itself [60-62]. Therefore, the commonality in all seven categories is the fabrication of the final desired part via the material deposition in a layer-by-layer progression [51].

2.1.1 LPBF Process Overview

From the seven main categories of AM processes, powder bed fusion (PBF) is a prominent technology in literature due to the ability to fabricate geometrically complex structures with excellent accuracy and exceptional design freedom [8, 9]. The PBF is a process that iteratively

utilizes a laser or electron beam to selectively melt and solidify a layer of powder to create a final structure. Figure 4 presents a schematic of the PBF AM process. Within the PBF process, the main components are the starting powder sitting in the powder reservoir, the recoating blade, a build platform and an energy source [63]. The PBF process begins with a coating blade spreading a uniform layer of powder on the build platform. Next, a focused high energy beam is rastered on the powder bed to melt and solidify the powder particles based on the imported CAD structure cross-section, concluding the first layer/iteration [60, 64]. The build platform is then moved downward, a height equal to that of the layer thickness, wherein a new layer of powder is layer on top of the first consolidated layer, and the energy beam is shined again to repeat the process [63].

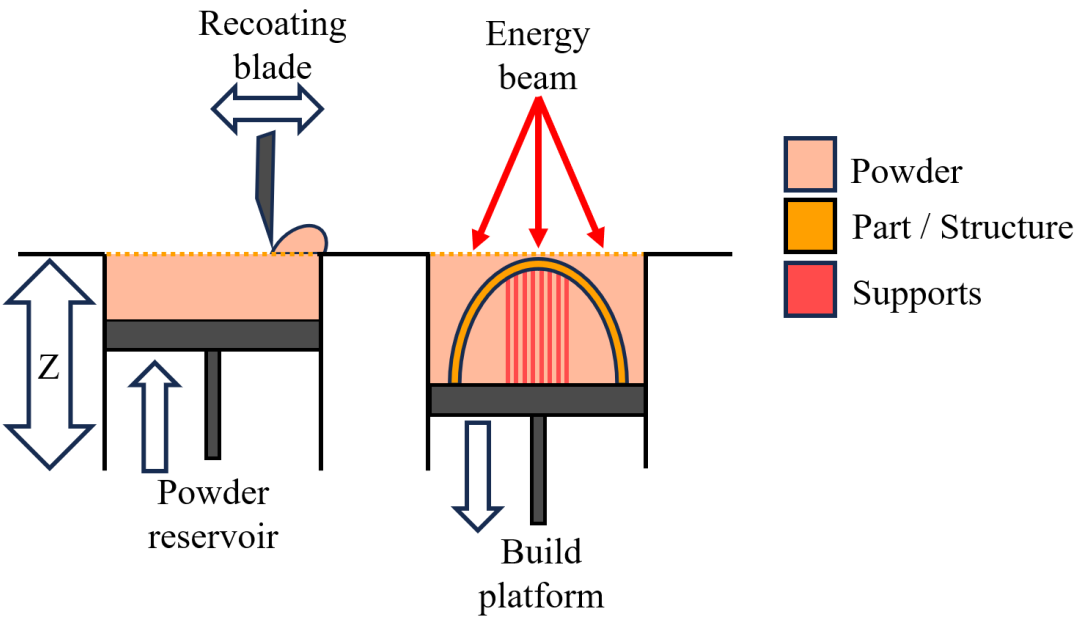

Figure 4. A schematic of a powder bed fusion (PBF) AM process.

Once the printing process is concluded, and printer is allowed to cool down to room temperature, the build platform is removed (including the fabricated structure on it) after the excess powder is removed [61, 63].

Withing the PBF family, two subcategories exist, with the main difference in the energy source. Electron powder bed fusion (EPBF), or electron beam – PBF, is a technology that utilizes a focused electron beam to melt and solidify metal and alloy powders. Due to the nature of the energy source, the EPBF process requires a vacuum environment during manufacturing [60]. On the other hand, LPBF, commonly referred to as selective laser melting (SLM), is a PBF AM technology that employes high energy laser beams as an energy source. With LPBF, a vacuum is not required, however, inert gases such as Ar and He are used to minimize powder oxidation during the manufacturing process [65]. Ultimately, the LPBF process appears to be the dominant PBF process most commonly used in both literature and industry applications.

Figure 5 presents a schematic visualization of the critical processing parameters of the LPBF process.

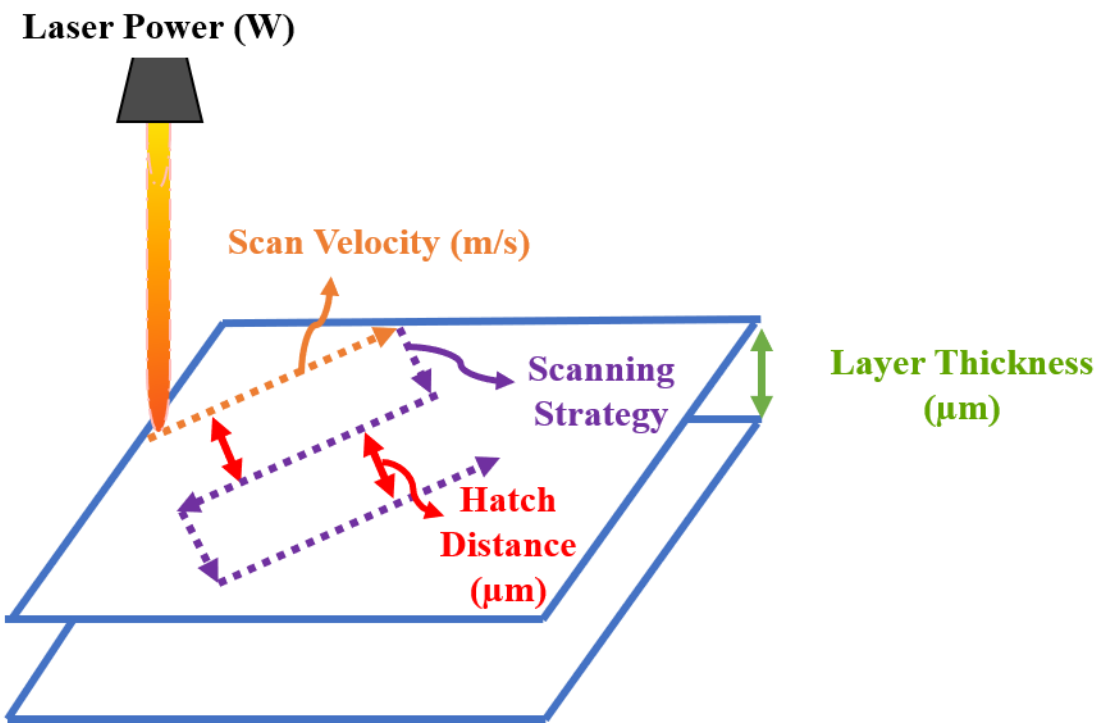

Figure 5. A schematic of the PBF printing parameters.

Below is the description of the most critical processing parameters of the LPBF process [60, 61, 63]:

2.1.1.1 Scanning strategy

A scanning strategy refers to the pattern and sequence used to build up a structure during an LPBF process. The selection of an appropriate strategy is of utmost importance as it controls the cooling time of melted layers and the overall properties of the built component [66]. An advantage of controlling the scanning strategy is the ability to control grain growth orientation and the final microstructural texture [67]. The effect on the scanning strategy is amplified once the build process goes from single to multi layer as the overlapping beads plays an essential factor in the cooling and solidification behaviours [66]. Studies by Su et al. [68] and Dewidar et al. [69] on the effect

of different scan strategies showed the direct effect between the selected strategy and the processing duration, deposited layer thickness, surface features, distortion and overall coherency of the build.

Figure 6 presents a schematic of 3 common scan strategies employed in LPBF of various alloys [70, 71]. In all strategies presented in Figure 6, the scanning vector of consecutive layers is rotated by (a) 90°, (b) 45° and (c) 67°. The aim behind the selection of such strategies is to increase the homogeneity of the energy input and solidification behaviour [66, 71-73].

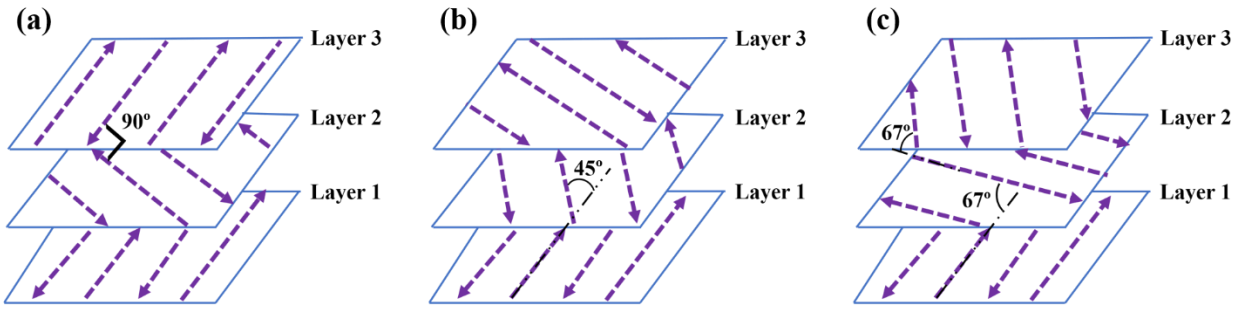

Figure 6. A schematic of common LPBF scanning strategies: (a) 90°, (b) 45° and (c) 67°.

Kruth et al. [74] suggests that the type of scan strategy and part geometry plays a direct role in the induction of internal stresses due to the formed temperature gradient. The authors summarized the observations based on the scan area: (1) A small scan area yields short scan length leads to overlapping scans with short cooling time, ultimately leading to high temperatures of the component, (2) A large area on the other hand, provides extended cooling time due to long scan lengths, leading to lower temperatures. In the case of larger scan area, the lower temperature leads to poor wetting conditions and lower thermal gradient, resulting in poor material density [66, 74].

Therefore, many studies were conducted on the effect of the scanning strategy and showed the ability to improve part density [75], surface quality [75, 76], wear resistance [77] and the elimination of entrapped gases [78] with the selection of the appropriate scan strategy [66].

Following are the most commonly discussed LPBF process parameters descriptions and effects on the final product:

2.1.1.2 Scan velocity, laser power and layer thickness

The scan velocity, laser power (i.e. laser energy input) and layer thickness are another set of parameters that are normally discusses in relation to each other in the LPBF processing parameters [66, 70].

Scanning velocity (m/s) is the velocity at which the laser beam moves along the lines of the scanning strategy [70]. This parameter is responsible for the interaction time between the input energy and the powder particles. Next, the laser power which dictates the laser energy input provides the heat to consolidate the powder particles on a powder bed. It determines the state of the recently consolidated particles, including sintering, melting and vaporization states respectively [66]. Finally, the layer thickness refers to the thickness of the powder layer place by the recoating blade during the printing process (Figure 5) [79].

A combination of a low laser power and scanning speed leads to low energy density (ED: J/mm^3) to form an adequate liquid phase, leading to poor densification of the fabricated part [66]. Combining high laser energy and low scan speed generates more heat at the powder bed, leading to significantly higher formation of liquid phase, resulting in improved densification due to the reduction of surface free energy [80]. Studies on the relationship between the laser power and scan

speed concluded that a carful control of the two parameters leads to improved densification through the reduction in liquid melt viscosity and surface tension [80, 81].

Finally, the combination of low laser power, high scanning speed and large layer thickness also leads to low input ED in the powder bed [66, 82]. In fact, with this combination, the ED is low due to the low laser power in addition to the short interaction time as a result of high speed (fast moving) scanning. Ultimately, the combination of these three settings lead to a limited interaction volume, leading to a lack of wetting, flowing, spreading, introduction of balling phenomenon and limited contact between the meltpool and solidified substrate [66, 83].

With regards to the layer thickness, a larger thickness leads to insufficient ED due to the large interaction volume, thus, low meltpool temperature, weak flow and balling phenomenon [83]. Although a larger thickness can generate a larger meltpool (with higher laser power), the simple distance between the meltpool and the solidified substrate leads to minimal contact area and adhesion of layers; in addition, melt track is reported to breakup due to the inability of small wetting areas to support larger meltpool [83]. Finally, layer thickness plays a direct role in the printing duration and part surface quality [66, 84]. Smaller thickness leads to longer build time and lower surface roughness, on the contrary, larger thickness leads to shorter build time and may cause stir-step effect, thus higher surface roughness [58, 84, 85].

2.1.1.3 Hatch distance

Hatch distance (HD: μm) is the distance between the sequential laser tracks of the as the laser follows the scan strategy (Figure 5) [84]. A small HD increases the overlap between the formed meltpools, reducing the meltpool depth, leading to less bonding between consecutive layers [66, 84]. However, a larger HD may not allow the meltpools to overlap sufficiently, resulting in

inadequate melting of the powder and porosity buildup [66, 84]. Nonetheless, studies on the effect of HD suggest the adjustment of HD to allow for 25% overlap between meltpools to eliminate the formation of pores and reduction in density [67].

2.1.1.4 Powder properties

2.1.1.4.1 Particle shape & density

The powder particle shape in another area of pre-manufacturing studies, as the shape of the particle dictates its flowability once a new powder layer is placed, the packing density and interaction with the energy source [66, 81, 86].

Irregular shaped powder particles, such as ones produced via water atomization for SS316L are regularly avoided in LPBF due to formed defects [87]. The defect caused by irregular powder particles are a result of inconsistent powder deposition (during recoating), ultimately due to low flowability and apparent density [88-90].

In addition, the shape of the powder and its apparent density have been shown to play a direct role in the absorptivity of a powder layer [91]. German et al. [92] reported that irregular powder morphology, characterized by high surface area per volume, has a tendency to absorb more thermal energy. A similar observation is reported by Tolochko et al. [93] and Yadroitsev et al. [91] where they report higher absorbance (A) for powder materials in comparison to bulk materials. The values were reported as follows: A_{Ti} bulk = 0.3, A_{Fe} bulk = 0.36, A_{Cu} bulk = 0.02 while A_{Ti} powder = 0.77, A_{Fe} powder = 0.64 and A_{Cu} powder = 0.59 at wavelength $\lambda = 1.06$ μm

Therefore, the typical powder feedstock in LPBF application consists of spherical shaped particles produced through atomization due to its satisfactory flowability, apparent density and final part density [86, 88].

2.1.1.4.2 Particle size distribution

Particle size distribution (PSD) is a powder property that presents the particle size and their frequency; it is commonly reported as D_{10}, D_{50} and D_{90} (μm) which corresponds to the size point below which 10%, 50% and 90% of the material is contained, respectively [94].

The PSD plays an important role in the determination of the powder packing density, flowability and the liquid phase condition [81]. With an uncontrolled PSD, complications such as balling, porosity, layer delamination and microstructural agglomeration may occur. Findings by Lumley et al. [95] reported that fine powders lead to the reduction in liquid quantity while coarse powders increased. Therefore, it is well established that a considerable difference in PSD may lead to segregation during the melting and solidification process [61]. Ultimately, the PSD can influence the chosen parameters of the LPBF process [66]. As an example, smaller sized SS316L powder yields near fully dense parts with a low energy beam intensity [96].

Typically, in a standard LPBF process, the powder presents spherical smooth morphology with a narrow range of particle size due to its improved flow, surface finish, hardness and mechanical properties [97].

2.1.2 LPBF Materials

The LPBF has been thoroughly studied on a wide variety of materials such as Al alloys for aerospace [10-12], Ti alloys for medical [13-15], Ni-based superalloys for jet engines and gas turbines [16-18] and Cu alloys for Defence [19-21] applications, respectively.

When it comes to the compatibility of a metallic/alloy powder with the LPBF process, there are two important factors the powders must satisfy: (1) Good wettability: to prevent the formation of cracks during the re-solidification of the material (2) Powder morphology: the ability to obtain spherical powders with adequate PSD to achieve proper packing density and deposition homogeneity [98].

Due to the possible change in the parameters during a LPBF process, the microstructure developed may vary [81]. The relationship between the input ED (i.e. laser power) and interaction duration (i.e. scan speed & strategy) dictates the operating environment via the temperature gradient (G), solidification velocity (R) and cooling rate (CR) [81, 99]. The following, equation 1, presents the relationship between G, R and CR [81] :

$$^{dT}/_{dt} = G \times R \qquad \text{Eq (1)}$$

Steen et al. [99] reported that increasing the G/R ratio leads to the gradual change from dendritic to cellular solidification regime; consequently, to planer growth. On the other hand, higher cooling rate results in finer microstructure through greater undercooling [81, 99]. Figure 7 presents a visualization of these findings. Therefore, several studies concur on the control of the resultant microstructure type and scale through the G, R and CR parameters [100-102].

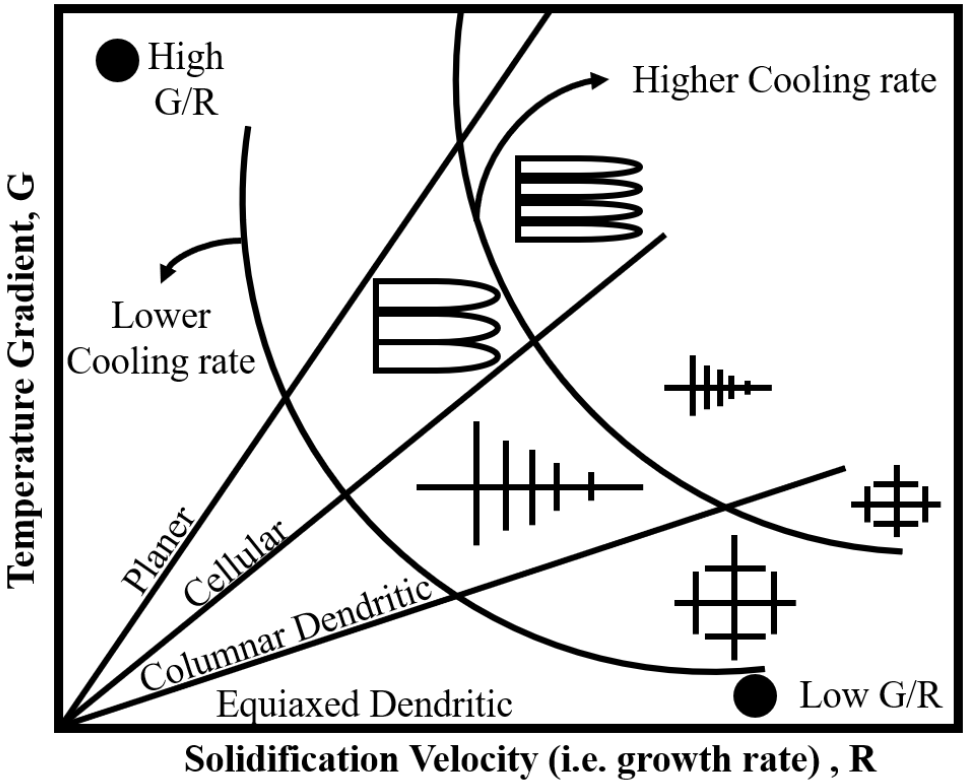

Figure 7. A schematic of the relationship between the temperature gradient (G), growth rate (R) and cooling rate (CR) on the resultant microstructure. Reproduced from [103].

Due to the range of G and R values during the LPBF process, thermal gradients (G) from the meltpool to the building substrate (heat escape path) results in a microstructure that resembles long columnar grains with a growth direction parallel to that of the build direction (BD) [62, 66, 70, 81]. As a result, anisotropy in mechanical property arise [60]. Common strategies used to overcome anisotropy include post-processing heat treatments and the adjustment of the scanning strategy [104-106]. Although heat treatments may eliminate the anisotropy produced by the long columnar grains by recrystalizing the matrix, the advantages of the fine LPBF structure may be dampened [107, 108]. Therefore, studies on the relationship between the scanning strategy and anisotropy

report that the scan strategy such as the 67° (Figure 6(c)) has been shown to inhibit the columnar grain growth while maintaining the favourable fine microstructure [70].

2.1.2.1 LPBF of SS316L

Within all families of metals used in LPBF, steels are frequently used in LPBF applications across a wide array. More specifically, LPBF of austenitic SS316L has generated significant attention due to its favourable mechanical properties, low density and excellent corrosion resistance [22-24, 60]. LPBF SS316L structures are utilized in several sectors, with applications in the marine, aerospace, energy and biomedical industries [109]. Table 1 presents the range of process optimization parameters typically used in literature.

Table 1. LPBF SS316L process optimization parameters.

Process Optimization	Layer Thickness	20 - 60 µm	[25, 110, 111]
	Scanning Speed	90 - 160 mm/sec	
	Density	65 - 99.9%	

2.1.2.1.1 Microstructure and Mechanical Properties

Table 2 presents typical characteristics and properties resulting from the process optimization.

Table 2. LPBF SS316L microstructure and mechanical properties.

Microstructure and Mechanical Properties	Cell Size	0.2 - 1 µm	[26, 27, 111-114]
	Hardness	172 - 282 HV	
	Tensile Strength	495 - 650 MPa	[111, 115, 116]
	Elongation	24 - 43.5%	

An average LPBF SS316L microstructure is comprised of meltpools, columnar grains and cellular sub-grain structure [111]. LPBF of SS316L shows improved mechanical properties compared to its wrought counterpart [22, 29], which is attributed to the smaller cell structure developed during the rapid melting and re-solidification events. The cellular sub-structure presents high density of dislocations, therefore, creating an obstacle for dislocation movement; Thus improving mechanical properties [111].

Despite geometrical complexity is achievable with AM processes, as discussed previously, anisotropy associated with long columnar microstructure presents a challenge for high-performance industries [103, 117]. Pitrmuc et al [118] reported differences in YS, UTS and elongation of LPBF manufactured parts as a function of the applied load direction. The authors reported a 20, 9, and 2% difference in YS, UTS and elongation, respectively, between horizontally and vertically built samples. Similarly, Tucho et al. [26] reported a 14% reduction in hardness at the cross-section (transverse) surface compared to surfaces perpendicular to the building direction. HT are known to mitigate these differences [31, 116, 119].

2.1.2.1.2 Post-Manufacturing Treatments

In efforts to improve the overall mechanical properties and the elimination of anisotropy, several publications have explored the effect of heat treatments on LPBF SS316L [25, 30-32]. The findings suggested recrystallization occurring between 1000 – 1200 °C [120-123] and resulting in a grain size ranging between 15 and 80 µm [25, 31, 32]. Minimising anisotropy through recrystallisation and grain growth however leads to a reduction in hardness and tensile strength (up to 27 and 48 % respectively) compared to as-build state due to the removal of the residual stresses, porosity, dissolution of cells, change in grain size and grain boundary density [25, 30-32, 124].

2.1.2.1.3 Oxidative performance

Oxidation resistance is another key property of SS316L ascribed to the Cr facilitating the development of a Cr_2O_3 oxide scale [33-37]. Vesel et al. [38] reported oxidation onset temperature of LPBF SS316L to be between 400 to 500 °C. Most oxidation works were conducted on vertically built samples between 700-1100°C and for durations of up to 500 hrs. The findings agree with parabolic oxidation kinetic laws and slower oxidation kinetics than the wrought counterpart [22, 39-41]. The reported chemical composition of the scales was consistent between the different works, resulting in Fe_2O_3 , Cr_2O_3 , Cr_2FeO_4 and Cr_2MnO_4 oxides development [22, 39-41].

2.1.3 The Economics of LPBF

The advantages of LPBF over TM is its ability to reduce lead time, labor and material cost [48]. However, these advantages are only significant in low – medium production volumes due to the incremental increase in used powder material during larger productions [125].

During a LPBF process, depending on the printed structure, a significant volume of the powdered material remains and is removed and collected at the end of the process to be recycled and reused [126]. The particle shape, PSD, surface morphology and composition are all important factors in the production of high quality and fully dense LPBF structures [126, 127]. Therefore, understanding the effect of powder reuse and storage is of upmost importance. These observations are not special to reactive metallic powders only, as the presence of the slightest oxidation strongly effects the resultant properties [128].

Despeisse and Ford [129] investigated the efficiency and sustainability aspect of AM processes. Their findings report that for metal AM processes such as LPBF, 95 – 98 wt.% of used powders may be recycled, therefore minimizing the material loss and improve the efficiency of the process [129]. However, powder degradation may occur due to the process environment and thermal cycles [126]. Studies on several metallic powders have shown that for reused powders, although the powder characterization are similar to that of the virgin powder, the microstructural and mechanical properties of final parts are scattered [126, 130]. The mechanical properties in specific have been shown to improve, decrease or be unaffected by the reuse of the powder material [130]. Studies by Slotwinski et al. [131] and Sartin et al. [132] concur on the increase of the SS316L PSD reused powder as the number of reuse cycles increased. Although the level of increase is material dependent due to the interaction with the laser, Ardila et al. [133] reported that for Inconel 718 powders, the increase in PSD was very minimal up to the seventh cycle. However, a shift in the rate of increase in the PSD value was observed between the seventh and fourteenth cycle.

Nonetheless, due to the complexity of the LPBF process and the several parameters to control, there is yet to have a concrete understanding of powder characterization and the degradation associated with the recycling of powders [126]. The presence of powder degradation limits the use of recycled powders to moderate applications as more complex applications such as ones in medical industries may not tolerate the negative impact on mechanical properties [61]. Therefore, limiting the ability to optimize cost effectiveness of LPBF process through material recycling.

2.1.3.1 LPBF Support Structure Cost Studies

Another approach in which cost optimization is approached is by optimizing the supports production and removal in LPBF parts [42, 60]. During the manufacturing process, downward-

facing surfaces of overhang structures are said to be self-supported at angles of 45° or higher (with respect to the horizontal axis) [134]. Therefore, low-angle (<45°) downward facing overhang surfaces require support structures to avoid geometric distortion, increased surface roughness and heat accumulation [134, 135]. The current works in literature regarding supports in LPBF generally fall in one of three categories [135-140]:

1. *Part cooling:*

   Supports structures play an important role in the conduction of heat from the meltpool to the substrate plate, thereby reducing the residual stresses developed through a stable thermal condition [135, 141]. A study by Kajima et al. [142] on Co-Cr-Mo LPBF structures printed at 45° angle reported the differences in microstructure and mechanical properties of the structure with and without supports. Supported samples presented fatigue strength twice larger than that of unsupported samples, as well as lower residual strain. These findings were attributed by the author to the finer grains of the and less defects and microcracks in the fracture surface of the supported sample [142]. A thermal simulation study by Chen et al. [143] on supported and unsupported overhang structures showed that supported structures presented with a lesser thermal gradient resulted in lower residual stress. This behaviour is attributed to the low thermal conductivity of the powder ($AlSi_{10}Mg$ powder: 8 W/mK) compared to consolidated supports ($AlSi_{10}Mg$ powder: 90 W/mK) [143].

2. *Geometric stability:*

   Part warping and distortion are two geometric failures that may be eliminated in LPBF with the use of proper support structures [135]. Liu et al. [144] reports a reduction in warping levels with the use of higher concentration of supports near the start and end of laser scans. On the

other hand, Kruth et al. [74] points out that higher support concentration leads to longer build times and complex support removal process. Yet, Pinto et al. [145] showed that a low support concentration leads to in-process failure as a result of increased possibility of particle clustering during initial layers. This observation led to the suggestion by Pal et al. [146] to optimize the interaction between the induced meltpool and the supports structures. Reducing the scan velocity reduces powder clustering is reported in LPBF Ti-Al_6-V_4 and SS316L [145, 146].

3. *Cost reduction:*

   Finally, the use of supports, instead of a solid bulk, decreases the overall cost through the lowered volume of consolidated powder used and the post-processing operations [135]. With the steady maturing of the LPBF technology, support generator software such as Sunata (Atlas 3D, Plymouth, IN), Magics (Materialize, Michigan, USA) and 3DXpert (3DXpert, Rock Hill, SC) were developed to allow user control over geometrical parameters of support structures [135]. Parameters such as support wall thickness and gap.

   Ultimately, by optimizing the support strategy, a cost reduction per part is achieved through lowering material used and post processing (support removal) [135].

2.1.3.1.1 LPBF Support-less Printing

As a result of the use of supports in LPBF, support removal post-processing steps are required to achieve the net-shape part. Since the fabrication of complex internal features one of the main advantages of LPBF, the removal of internal supports presents an expensive, time-consuming challenge [60, 135].

To highlight the economic impact of support removal post-process, Figure 8 presents the cost contribution of the design, manufacturing and support removal processes of overall support structure cost, as reported by Bartsch et al. [42]. The figure highlights that for a small number of parts, the manufacturing cost dominates the total cost of support structures. Nonetheless, with the increase in the number of parts built per job, the supports removal process becomes increasingly significant [42].

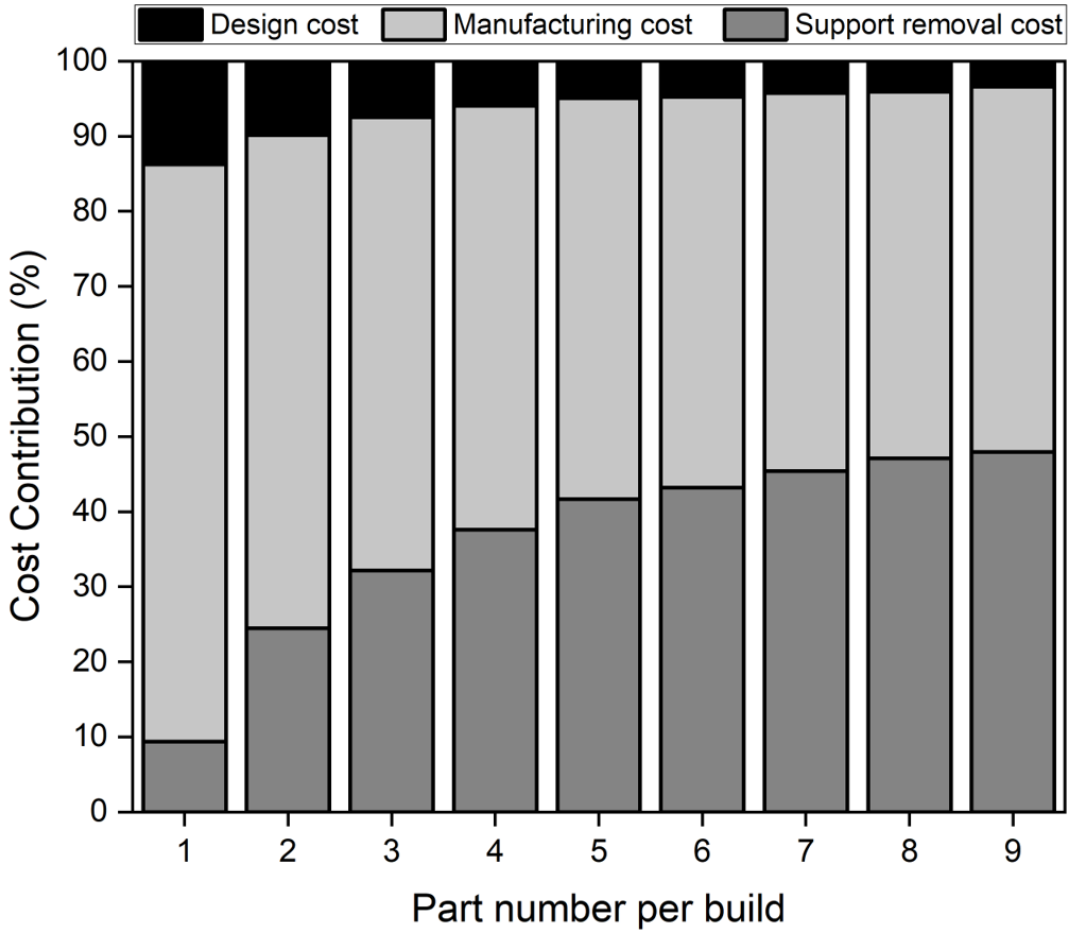

Figure 8. The cost contribution of the design, manufacturing and support removal processes to the overall support structure cost. Adapted from [42].

Therefore, establishing economically viable business cases for LPBF has driven the field to develop protocols with reduced supports and/or supportless printing for overhang structures

(downward-facing surfaces). Supportless printing, however, results in a local mismatch in microstructure compared to the bulk through the formation of a downskin [43-45]. The formation of downskin has only been recently explored due to the inherent complexity of supportless low angle overhang printing. The downskin is described as the formation of enlarged microstructure due to the heat accumulation at the substrate/powder interface [46]. The rise of distinct microstructure within the downward facing surfaces therefore results in a mismatch in mechanical properties between the bulk and downskin as reported by Kumar et al. [43] and Viale et al. [44].

Investigating the microstructural and mechanical properties of internal support-free IN625 LPBF parts, Kumar et al. [43] reported a have shown a downskin layer (300-500 μm thickness) of coarsened microstructure seven times larger than that of bulk surfaces, in addition to 21% drop in microhardness values at downskin surfaces compared to that of the bulk. The difference in microstructure may impact the component surface behavior during service, particularly in oxidation.

Nonetheless, studies conducted on the effects of LPBF supportless low-angle overhang printing has been limited to establishing the process parameter protocols for successful support-free printing [44] and its effects on dimensional tolerances and surface properties [45].

Chapter 3 Research Methodology and Results

3.1 Materials, Instruments and Experimental Procedure

3.1.1 Materials

3.1.1.1 SS316L Powder

Gas-atomized SS316L powder, sourced from Renishaw (UK), was used to fabricate the inverted hemispherical shaped part, name therein domes. Table 3 presents the composition of the powder as per the certificate of conformity provided by the supplier. Figure 9 presents a SEM micrograph of the starting powder showing mainly a spherical morphology with a few satellites.

Table 3. The chemical composition of the starting SS316L powder.

Elements	Fe	Cr	Ni	Mo	Mn	Si	C	N
Composition (wt%)	Balance	17.7	12.6	2.3	1.1	0.62	0.02	0.09

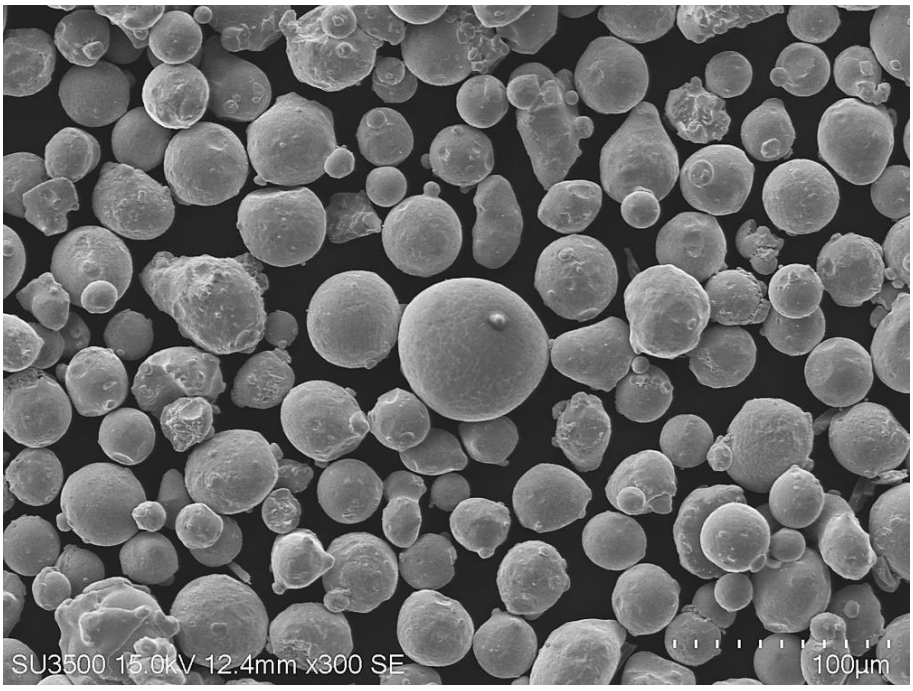

Figure 9. SEM micrograph of the starting SS316L powder.

3.1.1.2 Particle Size Distribution Analysis

The PSD was measured using the LA-920 Horiba laser particle size analyzer. The principal diameters D_{10}, D_{50} and D_{90} are 23, 34, and 51 µm, respectively.

3.1.2 LPBF System

Support-free domes of 10, 15 and 20 cm in diameter and 3 mm in wall thickness were fabricated. The domes were printed using a Renishaw AM250 equipped with a 200 W Nd: YAG laser. To avoid oxidation of the parts during printing, the process was conducted in an Ar atmosphere and an oxygen content below 300 ppm was maintained during the printing process. The scanning strategy consisted of a 67-degree rotation per layer, while the printing layer thickness was 30 µm.

Figure 10(a) presents a picture of the printed parts, while Figure 10(b) shows the CAD with the locations where the samples were extracted for analysis. In the present study, only the results of the 20 cm dome will be described to avoid redundancy, as they represent the most critical scenario of the three printed domes. Figure 10(c) closely presents the four locations of interest that are the (a, c) inner and (b, d) outer sides of the sections for printing angles of 90 (vertical printing) and 0° (horizontal printing). The following nomenclature: 90° inner, 90° outer, 0° upskin and 0° downskin will be used therein.

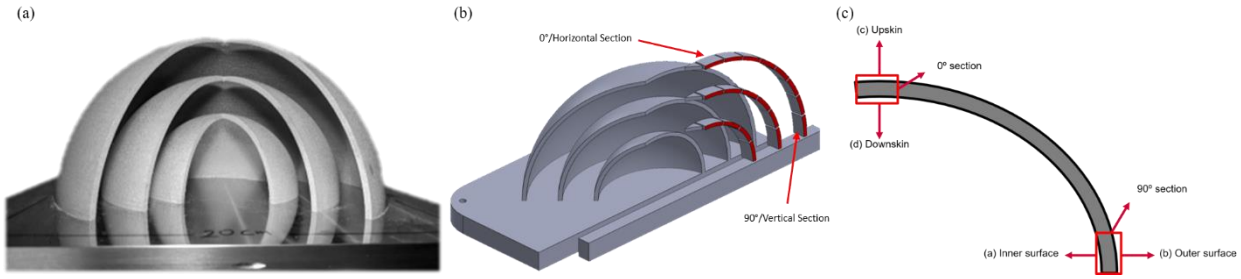

Figure 10. (a) Picture of the printed domes, (b) CAD representation of the printed domes showing the sample extraction and (c) four locations of interest for this study.

3.1.3 Sample Preparation

3.1.3.1 Sample Extraction

Sections of the domes were extracted from the built plate using a conventional band saw. The further sectioning of the specimen was performed using a Buehler Abrasive saw.

3.1.3.2 Heat Treatment

Two conditions were studied for these four locations: AB and HT. The heat treatment was full annealing, consisting of a soak at 1050°C for 1 hour followed by uncontrolled furnace cooling. The heat treatment was conducted in an MRF (Model: F-14x14x14-MM-1600-VT-G-HMI) furnace, reaching vacuum pressure levels of 10^{-6} Torr.

3.1.3.3 Oxidative Treatment

The AB and HT samples were oxidized in a Lindberg/Blue (BF51800) box furnace at 900 °C for 100 hours in dry air, followed by furnace cooling. The samples were inserted at room temperature

prior to heating to the set temperature. In order to understand the effect of the grain size on the developed scale thickness, one sample was heated to the oxidation temperature (900°C) in the same conditions. Upon reaching the temperature, the furnace was immediately turned off (no dwell time) to let the sample to cool. This sample will be referred to as T_0 oxidation sample.

3.1.3.4 Mounting and Polishing

The sample preparation involved mounting in Technotherm 3000 resin, followed by grinding up to 800 grit sic abrasive paper and standard polishing using diamond suspensions of 9 μm, 3 μm and 1 μm. A Vibromet 2 was used to perform the final polishing step with 0.05 μm colloidal silica suspension.

3.1.3.5 Etching

In order to conduct a microstructural analysis of the surfaces of interest, an electrochemical etching process was used to revealed the developed microstructure. The electro-etching procedure was done with the samples submerged in a solution of 10% oxalic acid at 3V for 25-30 s.

3.1.4 Microstructural Characterization

3.1.5.1 Secondary Electron Microscope

A Hitachi SU3500 SEM was used for higher magnification analysis of the etched microstructure present in the AB state. In addition, the SEM was used to capture the T_0, and oxide scales developed in the AB and HT conditions. With all collected micrographs, ImageJ software was used to measure the different microstructural features.

3.1.5.2 Optical Microscopy

A Keyence VHX 5000 digital light optical microscope (OM) was used for optical imaging of the HT etched surface. Similarly, ImageJ software was used to measure the different microstructural features.

3.1.5.3 Electron Backscatter Diffraction

To further understand the effect of the applied heat-treatment on the matrix, electron backscatter diffraction (EBSD) analysis was conducted to analyze the grain morphology and crystallographic texture. The EBSD maps were obtained at 15 kV and 3 μm step size, where the indexing rates were kept above 85% throughout the EBSD map.

3.1.5.4 X-Ray Diffraction

After the applied oxidative cycle, the samples were analyzed via x-ray diffraction (XRD) in order to identify the developed phases during oxidation. The present phases were identified using a Bruker D8 Discovery X-Ray diffractometer (Germany) equipped with a Cobalt (Co) anode (Kα1

wavelength, λ = 1.7890 Å). The diffraction data was acquired between 2θ values of 35° and 95° on three frames using 200s/frame. The Crystallography Open Database (COD) was used for peak identification.

3.1.5.5 Energy dispersive X-ray spectroscopy

To further understand the structure in which the oxide scale is developed, chemical mapping of the oxide scale was done using Energy dispersive x-ray spectroscopy (EDS) analysis. For chemical identification, Oxford's Aztec data acquisition was used.

3.1.5 Mechanical Property Characterization

3.1.6.1 Microhardness Testing

Vickers microhardness measurements were acquired on a Clark CM-100AT (Sun-tec, USA) automated microhardness indenter using a 200-gf load and 15 s dwell time. The reported measurements are an average of 6 indents. Figure 11 presents the microhardness testing strategy used in the present study. For all surfaces, the indents were set at equidistant from each other. However, considering the irregularity and roughness of the downskin surface, the indents were adjusted to maintain 150-200 μm away from the edge of the sample.

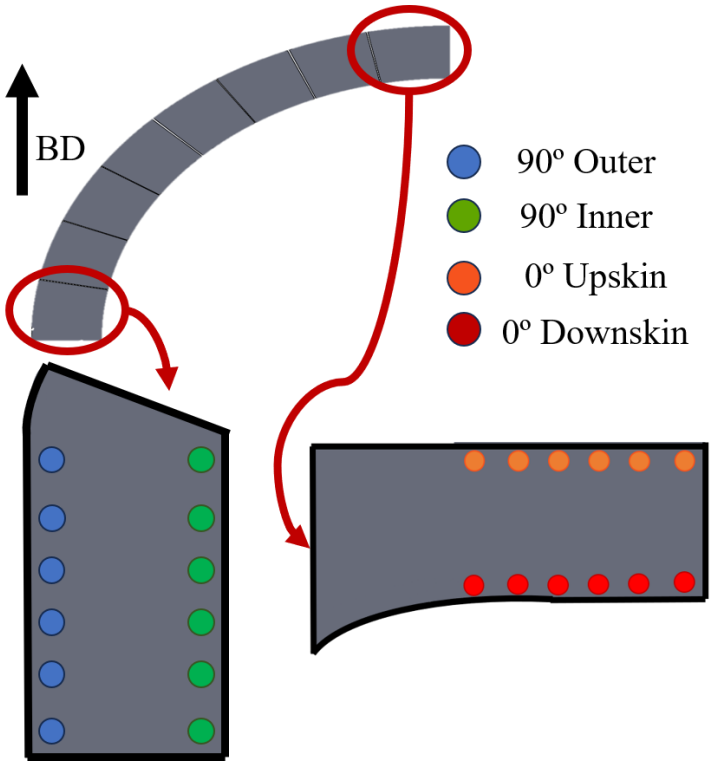

Figure 11. Microhardness testing strategy used in the present study

3.2 Results

3.2.1 Microstructural and Mechanical Characterization

3.2.1.1 As Built Condition

Figure 12 presents SEM micrographs showing the etched AB microstructure of the (a) 90° inner surface, (b) 90° outer surface, (c) 0° upskin and (d) 0° downskin locations, respectively.

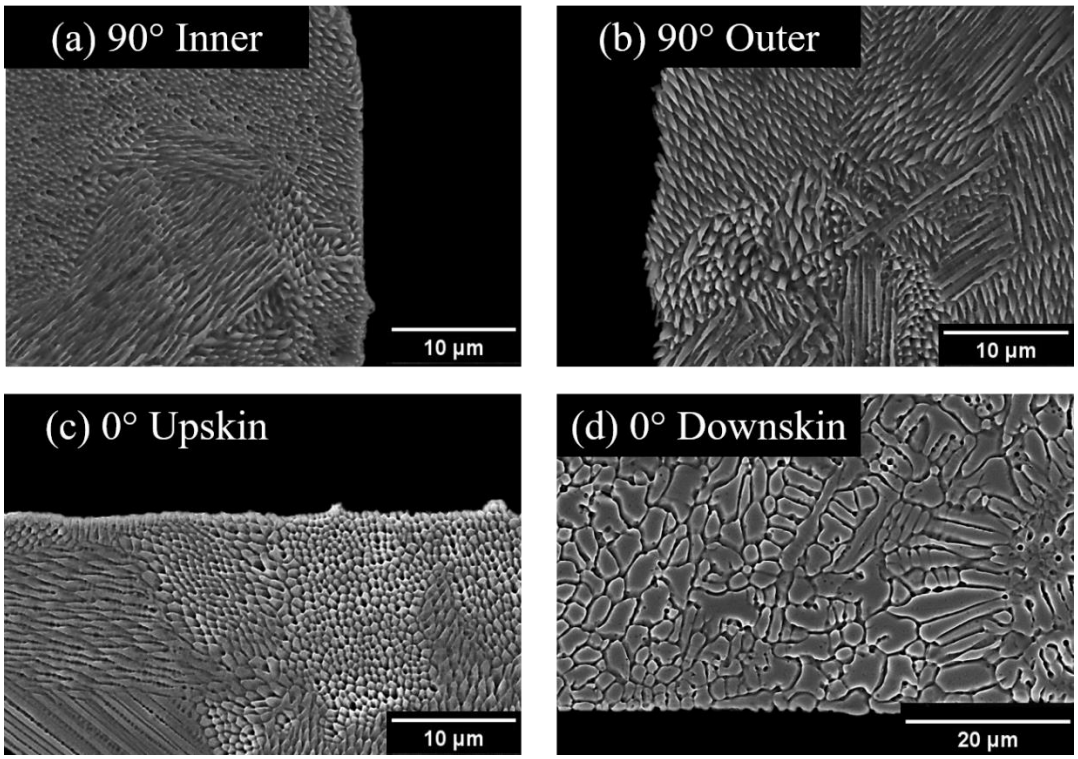

Figure 12. AB microstructure of the (a) 90° inner surface, (b) 90° outer surface, (c) 0° upskin and (d) 0° downskin.

Table 4 presents the cell size measured for the four locations. Regarding the vertical inner and outer locations, the cell sizes were 0.76 ± 0.07 and 0.71 ± 0.10 µm, respectively. The student T-test suggested that for a $p<0.05$, the two populations of cell size are similar. Unlike the vertical section, the horizontal section contains two distinct microstructure length scales corresponding with the upskin and downskin. The cell size observed in the upskin section was 0.69 ± 0.09 µm

while a dendritic structure with a size of 3.19 ± 0.20 μm was measured for the downskin. The student T-test suggested that for a $p<0.05$, the two populations are different. Upon closer examination of the downskin microstructure presented in Figure 12(d), the presence of secondary dendrite arms is observed, measuring 0.99 ± 0.18 μm.

Table 4. Cell size and microhardness measured from the different locations of the AB dome

Location	Surface	Measured Feature	Cell size (μm)	Cooling Rate (k/s)	Microhardness
90° wall	Inner	PDAS	0.76 ± 0.07	1.36×10^6	247 ± 6
	Outer	PDAS	0.71 ± 0.10	1.65×10^6	246 ± 4
0° location	Upskin	PDAS	0.69 ± 0.09	1.80×10^6	239 ± 4
	Downskin	PDAS	3.19 ± 0.20	1.74×10^4	225 ± 3
		SDAS	0.99 ± 0.18	1.81×10^4	

Table 4 presents the microhardness data for the four studied locations, and the results are 247 ± 6 HV for the 90° inner, 246 ± 4 HV for the 90° outer, 239 ± 4 HV for the 0° upskin surface 225 ± 3 HV for the 0° downskin surfaces, respectively. Due to the formation of a coarser solidification structure, the microhardness value drops by an average of 14 – 22 HV (6 – 9%) between the vertical/0°upskin locations and the 0° downskin location.

3.2.1.1.1 Electron Backscatter Diffraction Analysis

EBSD analysis was carried out to better understand the microstructure of the AB state. Figure 13 presents EBSD inverse pole figure (IPF) maps of the AB (a) 90° inner, (b) 90° outer, (c) 0° upskin, and (d) 0° downskin surfaces, respectively. In addition, the pole figure (PF) maps of the IPF maps are plotted for [1/00], [/110] and [1/11] planes along the build direction are also shown. The red and blue colors within the PF represent the maximum and minimum intensity of the multiple uniform densities (MUD).

Using the EBSD micrographs presented in figure 23, the grain size of the AB bulk (Figure 13(a, b and c)), transition (Figure 13(d)) and downskin locations (Figure 13(d)) are measured at 26 ± 3 µm, 35 ± 15 µm and 11.5 ± 5 µm respectively.

Figure 13(d) focuses on the 0° downskin location, where three regions can be identified, all presenting a different microstructure. The upper section of the micrograph presents a microstructure and texture similar to that of the bulk and the other three studied locations i.e. inner/outer/upskin. The grain size of the AB bulk measured from Figure 13(a, b and c) and the top section of Figure 13(d) is at 26 ± 3 µm with a grain aspect ratio (AR) of 2.5 ± 0.3. Closer to the surface, a transition region emerges, exhibiting a microstructure which is neither that of the bulk or the downskin due to the increased heat extraction (compared to the downskin) through the previously consolidated layers. The grain size of the transition region is measured at 35 ± 15 µm, with AR of 2.5 ± 0.9. Finally, the last region called DS is the initial 250 - 300 µm from the outer surface, the observed texture resembles equiaxed grains, with grain size of 11 ± 5 µm and an AR of 1.4 ± 0.3. This equiaxed texture arises due to the unique combination of temperature gradient (G) and solidification velocity (R), leading to extended solidification time.

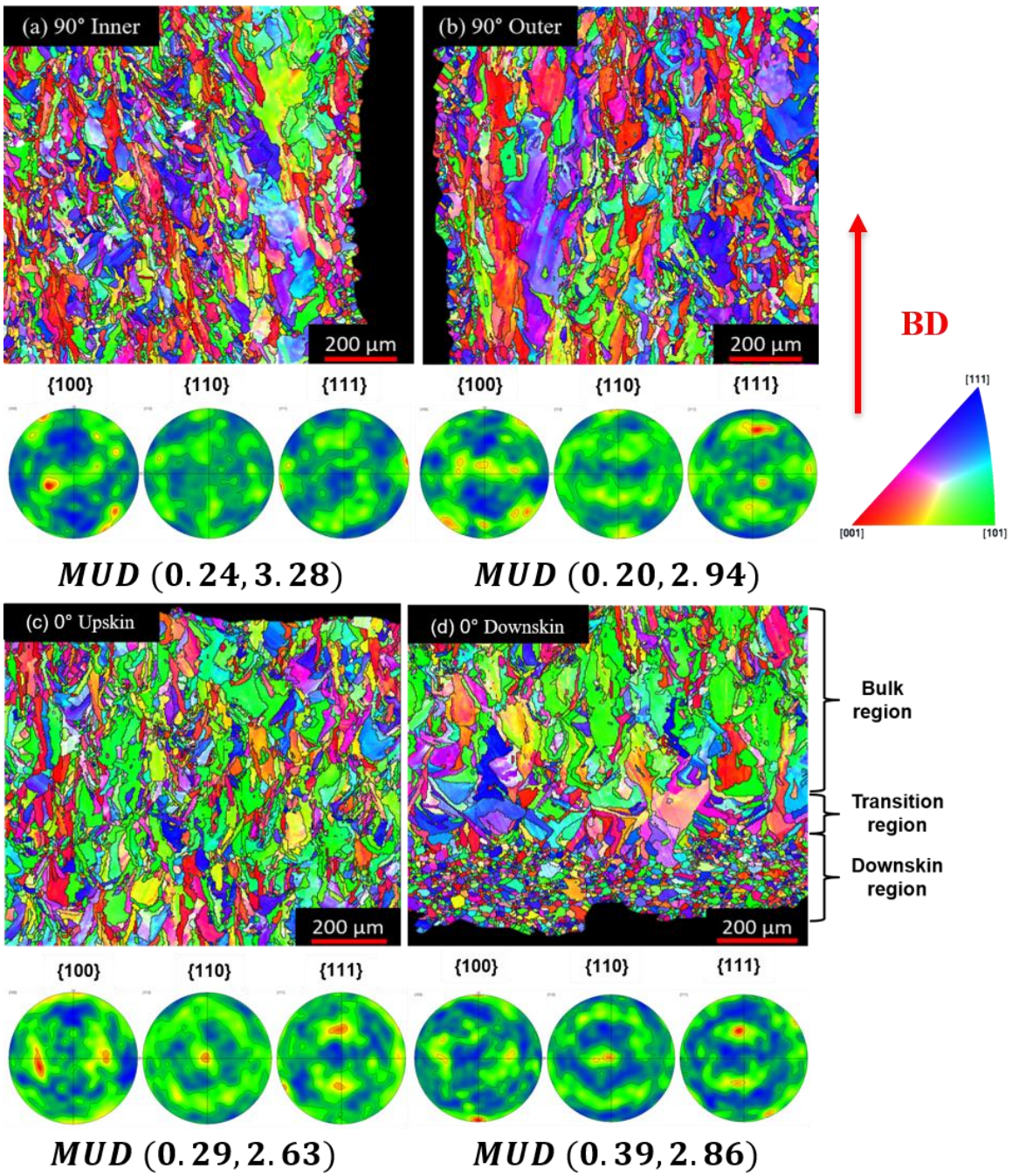

Figure 13. The EBSD map (IPF-Z) of the four AB locations of interest. From left to right, the PF are corresponding to the [100], [110] and [111] planes along the build direction.

3.2.1.2 Heat Treated Condition

Figure 14 displays optical microscopy micrographs presenting the etched HT microstructure at different locations: (a) 90° inner, (b) 90° outer, (c) 0° upskin, and (d) 0° downskin surfaces, respectively. The heat treatment process causes the transformation of the long columnar grain structure in the AB state into larger grains with random orientations through solutionization and recrystallization. Table 4 presents the grain size measurements for the four analyzed locations.

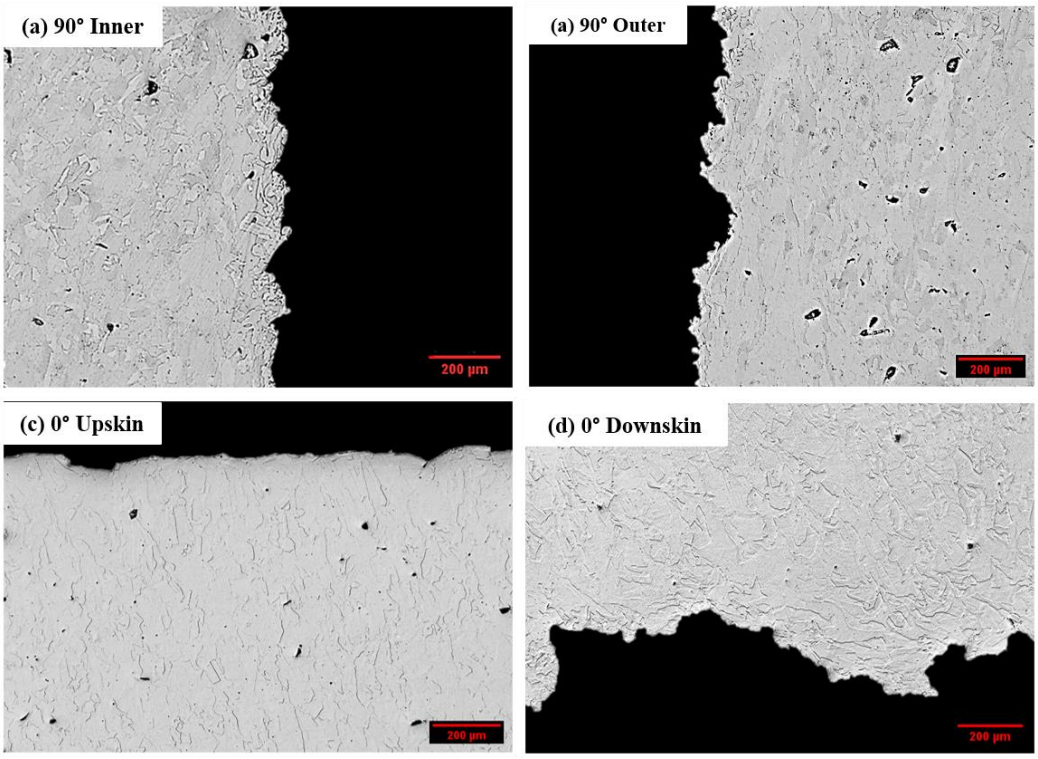

Figure 14. Etched HT microstructure of the (a) 90° inner surface, (b) 90° outer surface, (c) 0° upskin and (d) 0° downskin surfaces.

Table 5. Grain size and microhardness measured from the different HT locations of the dome.

Location	Surface	Grain size (µm)	Microhardness
90° wall	Inner	30 ± 3	188 ± 4
	Outer	31 ± 3	183 ± 3
0° location	Upskin	33 ± 2	181 ± 4
	Downskin	26 ± 3	195 ± 3

Regarding the locations depicted in Figure 14, the grain size for the HT 90° inner, 90°outer, 0° upskin and 0° downskin regions measured 30 ± 3, 31 ± 3, 33 ± 2 and 26 ± 3 µm, respectively. The one-way ANOVA test for $p<0.05$ suggest that the grain size measurements for the vertical and upskin HT locations (Figure 14(a, b and c)) were statistically similar while the downskin location (Figure 14(d)) presents a statistically smaller grain size. When compared to the AB condition, the HT microstructure has experienced a slight grain growth, where the grain size increased from 26 microns to 30-33 microns for the 90° inner, 90°outer, 0° upskin. Grain growth occurred in the downskin region, increasing from 11 to 26 microns.

Microhardness testing was performed to investigate the effect of the heat treatment on the local mechanical properties. Table 5 presents the microhardness data for the four studied locations, and the results are 188 ± 4 HV for the 90° inner, 183 ± 3 HV for the 90° outer, 181 ± 4 HV for the 0° upskin and 195 ± 3 HV for the 0° downskin surfaces, respectively. The one-way ANOVA test for $p<0.05$ suggests that the microhardness measurements for all three bulk HT locations (vertical/upskin locations) were statistically similar. While for the downskin location, similar to the trend observed in the AB condition, the microhardness measurement presents a different range post heat treatment compared to the bulk locations. In the AB condition, the microhardness observed in the downskin is less than that of the bulk. However, post heat treatment, the

microhardness measurement in the downskin location is larger than that of the bulk. In comparison to the AB condition, the mean microhardness value across the bulk locations post heat treatment is 184 ± 4 HV, approximately 60 ± 1 HV (28%) lower than that of the AB state. While for the downskin location, the microhardness value is approximately 30 ± 1 HV (14%) lower than that of the AB state. The drop in microhardness measurement value follows the relationship established by the Hall-Petch effect.

3.2.1.2.1 Electron Backscatter Diffraction Analysis

To better understand the effect of the heat treatment, the microstructure was characterized by EBSD analysis. Figure 15 presents an EBSD map of the HT (a) 90° inner, (b) 90° outer, (c) 0° upskin, and (d) 0° downskin surfaces, respectively. The effect of the heat treatment can be seen in terms of larger and randomly oriented grains. Unlike in the AB state, where the MUD value was a maximum of 3.28, after the heat treatment, the MUD value for the bulk locations remained at and under 2.90; Suggesting an increased level of randomness of the texture. From Figure 15(b), although the gains at the bulk of the sample are observed to be semi-equiaxed and randomly oriented, grains closer to the surface are seen to sustain the long columnar along the build direction. A similar observation can be made with maps presented in Figure 15 (a, c and d). These observations suggest insufficient temperature and time elapsed to induce a uniform recrystallization throughout the samples.

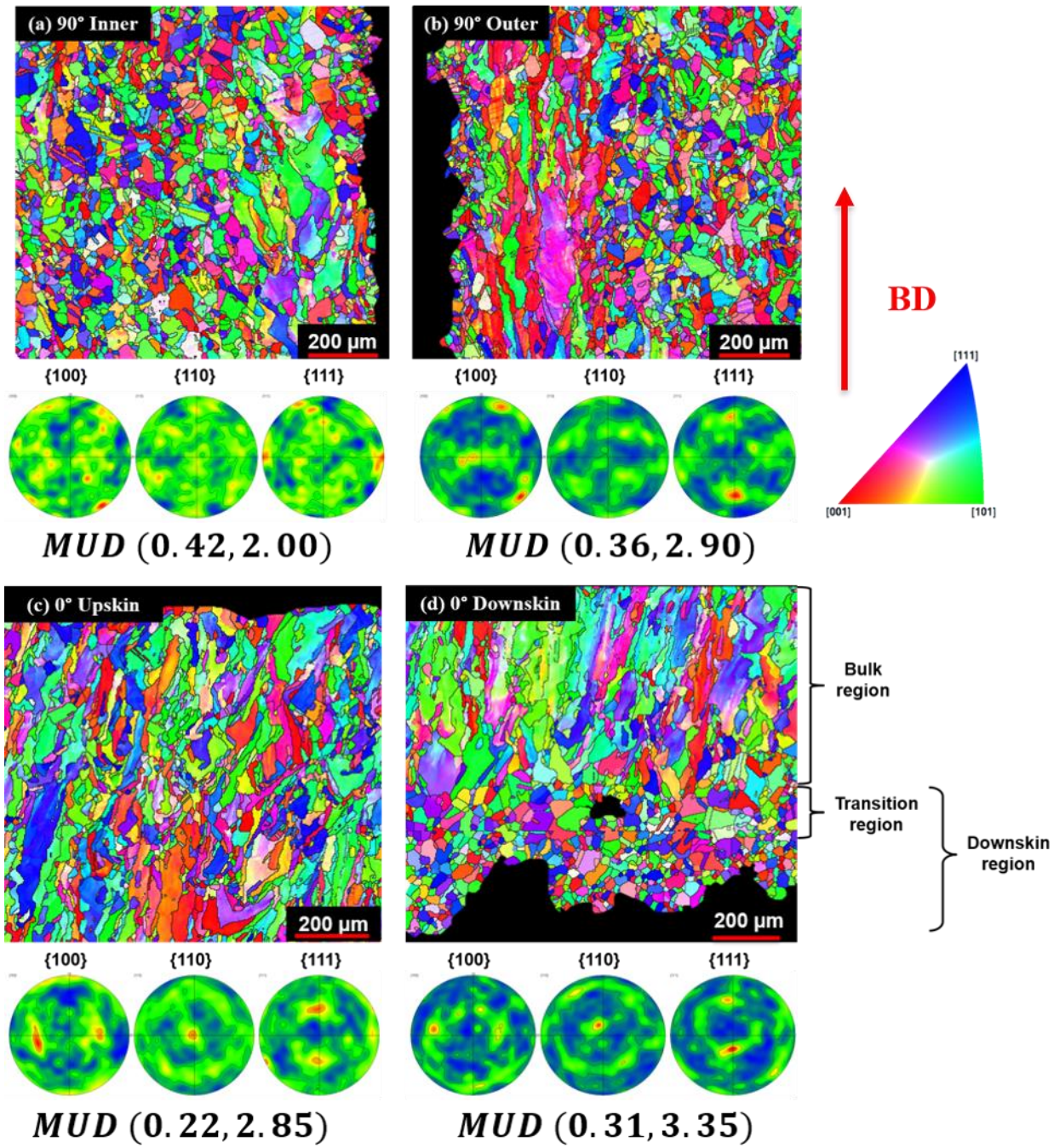

Figure 15. The EBSD map (IPF-Z) of the four HT locations of interest. From left to right, the PF are corresponding to the [100], [110] and [111] planes along the build direction.

3.2.2 AB vs. HT Oxidation Response

To understand the microstructure evolution during the oxidation process, the microstructure of the sample corresponding to a heating in Ar up to 900 C followed by immediate cooling and without any exposure to air was first investigated to evaluate if any microstructure change is occurring during the ramp-up. Figure 16 presents the SEM micrographs of (a) the upskin (representing the bulk) and (b) the downskin microstructure. The cellular microstructure remained for both locations despite the heating. The calculated PDAS was 0.68 ± 0.03 and 3.24 ± 0.38 µm for the bulk and downskin, respectively. The student T-test suggested that for a $p<0.05$, the populations of cell size in the AB and T_0 conditions are similar for both the bulk and downskin PDAS values.

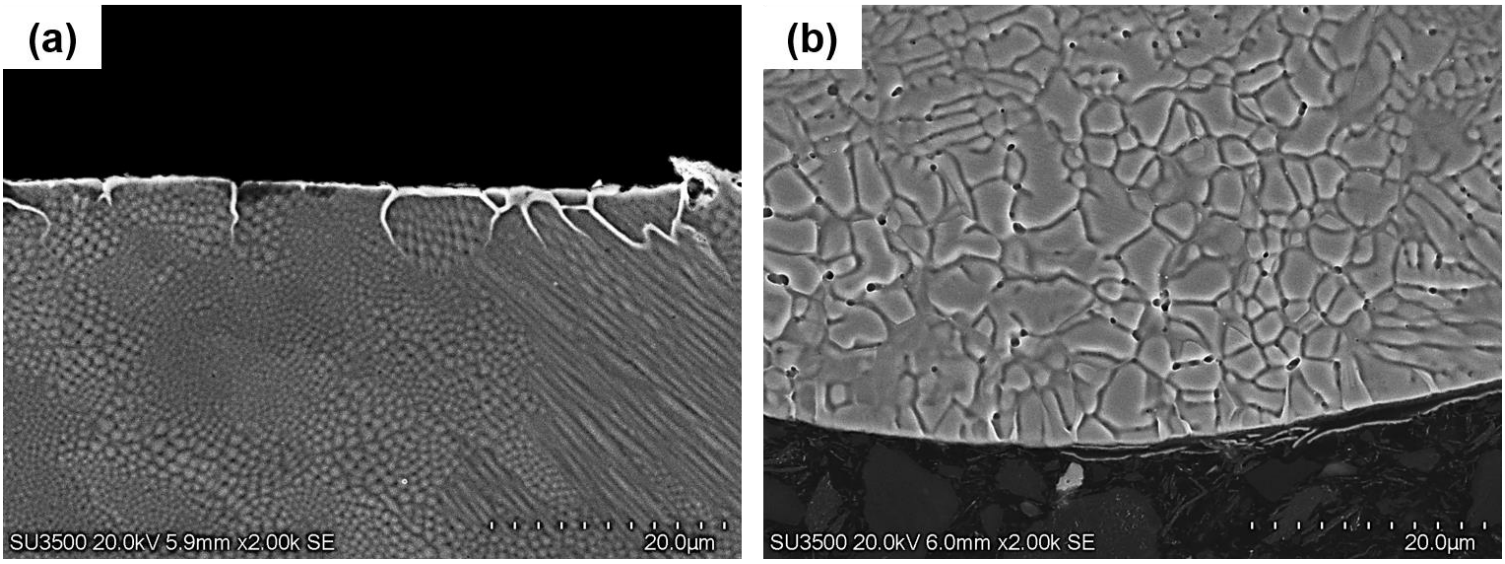

Figure 16. Etched T0 microstructure of the (a) Bulk and (b) Downskin surfaces.

3.2.2.1 X-Ray Diffraction

Figure 17 presents the XRD spectra of the oxide scales developed on the (a) AB and (b) HT samples after 100 hours at 900°C in a dry air environment. The XRD results show that for the four locations, regardless of the sample condition, the developed scales are composed of the same oxide stoichiometries, which are Fe_2O_3 (PDF: $04-006-6579$), Cr_2O_3 (PDF: $04-025-2779$), Cr_2FeO_4 (PDF: $04-016-4072$) with a minor presence of Cr_2MnO_4 (PDF: $04-002-1873$).

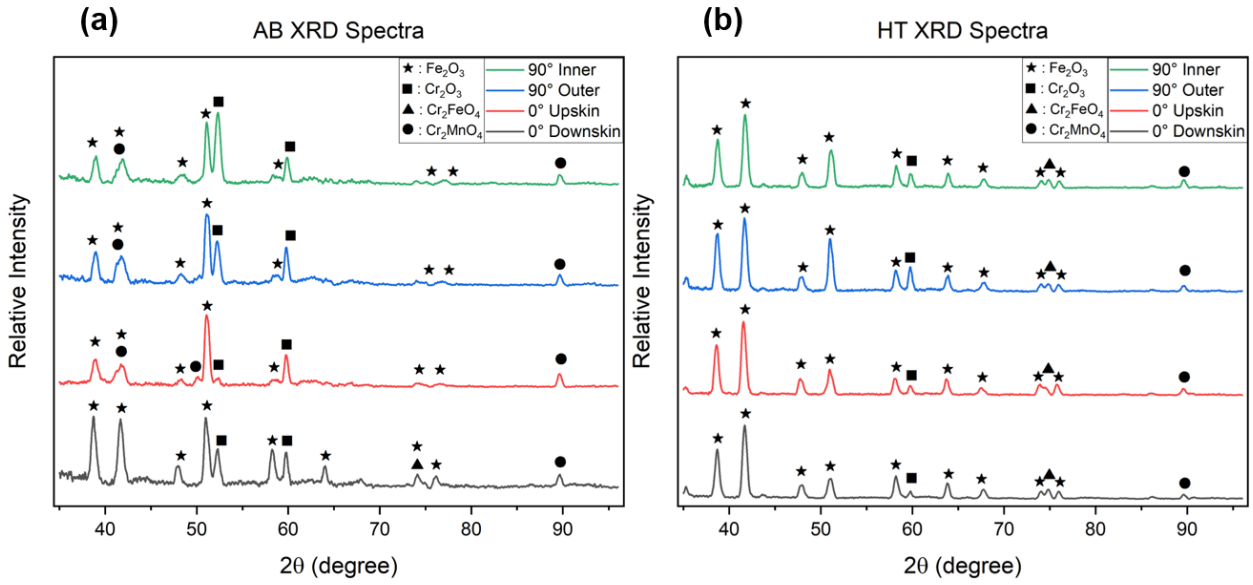

Figure 17. The (a) AB and (b) HT XRD spectra at the four locations of interest.

3.2.2.2 Energy dispersive X-ray spectroscopy Analysis

Chemical mapping using EDS was performed to understand the layering of the oxides in the scales. Figure 18 presents respectively a BSE micrograph with the chemical maps for O, Fe, Cr, Mn and Si for the AB (a) 90° inner, (b) 90° outer, (c) 0° upskin (d) 0° downskin and HT (e) 90° inner, (f) 90° outer, (g) 0° upskin (h) 0° downskin surfaces, respectively. The chemical distribution suggests a two-layer oxide scale evolution for all samples, either in the AB and HT states. The inner and outer layers are identified as Cr_2O_3 and Fe_2O_3 oxides, matching the XRD results presented in Figure 17. The EDS micrographs presented in Figure 18 also reveal specific regions where oxygen diffuses inwards beyond the formed oxide scale (indicated by red arrows). These linear features correspond to the grain boundaries in the material. Upon closer examination of the Fe and Cr EDS maps depicted in Figure 18, Fe depletion region following the grain boundaries is evident. Additionally, a slight reduction in Cr intensity can also be observed with these grain boundary regions.

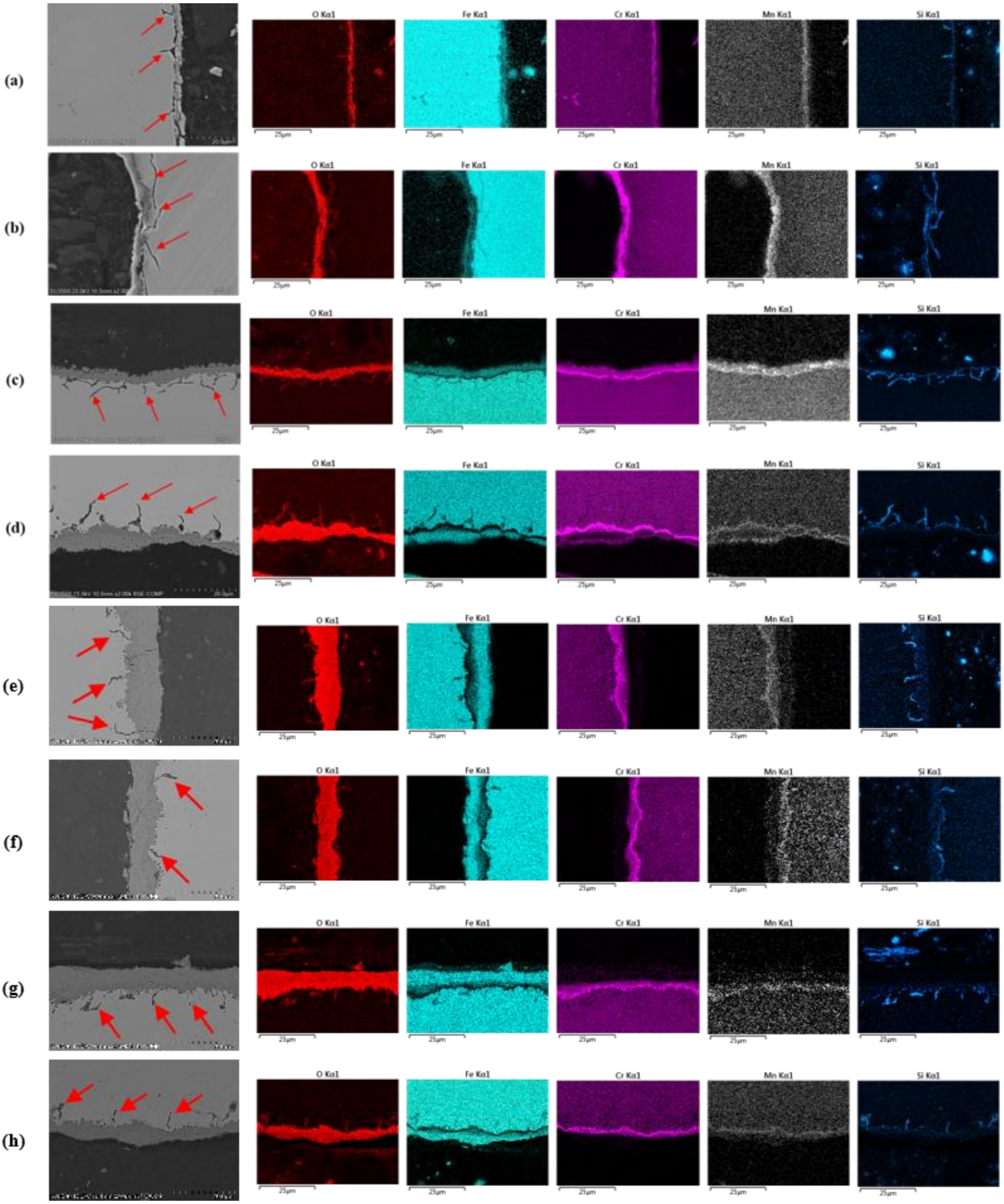

Figure 18. BSE (left) and EDS (right) analysis results presenting the oxide layer micrograph and composition at AB (a) 90° inner surface, (b) 90° outer surface, (c) 0° upskin, (d) 0° downskin and HT (e) 90° inner surface, (f) 90° outer surface, (g) 0° upskin, (h) 0° downskin. From left to right, the EDS chemical maps correspond to O, Fe, Cr, Mn and Si respectively.

3.2.2.3 Oxide Scale Thickness

The oxide scale thickness was measured at the four AB and HT locations, providing beneficial insights into the oxidation resistance of the four surfaces. Table 6 presents the oxide scale thickness at the four locations in the AB and HT state. For the AB state, the average measured oxide thickness for the 90° inner, 90° outer, 0° upskin, and 0° downskin surfaces are 3.4 ± 1.2, 3.9 ± 1.7, 3.8 ± 2.2, and 3.8 ± 1.8 µm, respectively. The one-way ANOVA test suggests that for a $p<0.05$, the oxide scale thickness developed at the four AB surfaces is similar. On the other hand, for the HT state, the average measured oxide thickness for the 90° inner surface, 90° outer surface, 0° upskin, and 0° downskin surfaces are 7.7 ± 3.3, 8.1 ± 2.1, 8.1 ± 1.8 and 7.1 ± 2.1 µm, respectively. The one-way ANOVA test suggests that for a $p<0.05$, the oxide scale thickness developed at the four HT surfaces is similar. This observation is attributed to the grain structure being in the micron-size and without the cellular structure post-HT.

Table 6. The oxide scale thickness measured at the four locations in AB and HT conditions.

Location	**Oxide scale thickness (µm)**	
	As Built (AB)	**Heat Treated (HT)**
90° inner	3.4 ± 1.2	7.7 ± 3.3
90° outer	3.9 ± 1.7	8.1 ± 2.1
0° upskin	3.8 ± 2.2	8.1 ± 1.8
0° downskin	3.8 ± 1.8	7.1 ± 2.1

Chapter 4 Discussion

4.1 Microstructural and Mechanical Characterization

4.1.1 As Built Condition

The four micrographs presented in Figure 12 displayed a typical cellular solidification sub-structure developing during LPBF of SS316L [23, 24, 113, 115, 147]. The averaged reported PDAS measurement in literature ranges between 0.3 and 0.9 μm [26, 27, 111-113, 134]. Therefore, the values reported in Table 4 for the 90° inner, outer and 0° upskin fall within the reported range. However, the downskin surface presented larger PDAS values in addition to the observed SDA formation. Ultimately, the formation of a dendritic structure (> 1 μm) at the downskin of a supportless structure is consistent with those reported by Viale et al. [44].

A similar trend is reported in a study conducted by Kumar et al. [43] who investigated the microstructural and mechanical properties of internal support-free IN625 LPBF parts. The authors reported a seven times larger values of PDAS in the downskin compared to the bulk; In addition to approximately 21% drop in the microhardness measurement in the supportless downskin location.

Figure 19 presents the Hall-Petch relationship of the measured microhardness and PDAS values, graph that is augmented with points from literature for comparison [27, 111-114]. The microhardness values obtained in the current study (Table 4) fall within the values reported in the literature, ranging between 210 and 280 HV [27, 111-114]. The microhardness of the bulk locations is higher in comparison to the downskin due to the higher grain boundary density and the cellular dislocation network which is stabilized during loading through the slight disorientation between

the developed cells [27, 144, 148-150]. Studies presenting different PDAS such as Sun et al. [112] and Wang et al. [27] show a clear relationship between the PDAS and the measured microhardness value. As the measured PDAS increases, the microhardness decreases; following the Hall-Patch relationship.

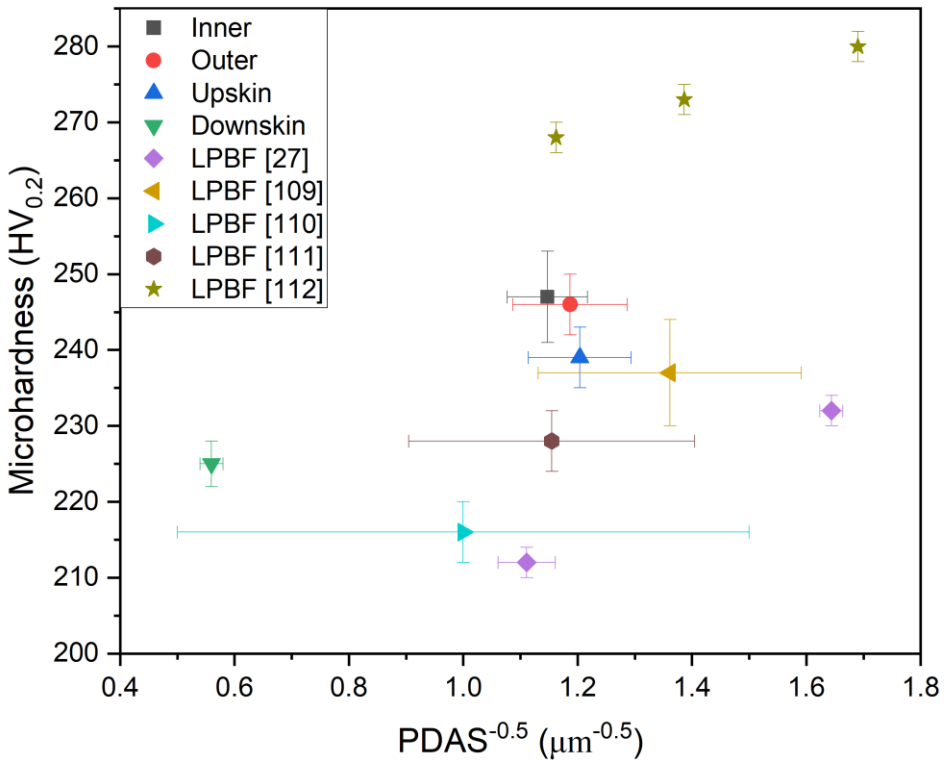

Figure 19. Microhardness as a function of the reciprocal of the PDAS for AB condition. Values from literature are plotted for comparisons. *Note: the downskin point has been plotted using the PDAS value.*

4.1.1.1 Estimation of Cooling Rate

To get an understanding of the solidification conditions, two approximation methods are used for the bulk and the downskin, respectively. The corresponding cooling rate associated with the measured PDAS values was calculated using Equation (2):

$$d = a\epsilon^{-b} \qquad \text{(Eq.2)}$$

where d is PDAS (μm), ε represents the cooling rate (k/sec), and a and b are constants. Specifically, for SS316L, the two constants are: $a = 80\mu m(k/s)\ and\ b = 0.33$ [151]. For the bulk locations (inner/outer/upskin), the average calculated cooling rate is 1.58×10^6 k/sec. For the downskin location, the calculated cooling rate is 1.74×10^4 k/sec. The summery of the calculated cooling rates is presented in Table 7.

Table 7. The measured cooling rate at each of the four AB locations.

Location	Surface	Measured Feature	Cooling Rate (k/s)
90° wall	Inner	PDAS	1.36×10^6
	Outer	PDAS	1.65×10^6
0° location	Upskin	PDAS	1.80×10^6
	Downskin	PDAS	1.74×10^4
		SDAS	1.81×10^4

Considering the microstructure of the downskin having SDAS, the regular regression used to calculate the cooling rate in casting and welding was also utilized for comparison. The cooling rate using the SDAS can be calculated using Equation (3) [152]:

$$\lambda = A(GR)^{-n} \qquad \text{(Eq.3)}$$

where λ is SDAS (μm), GR represents the cooling rate (k/sec), and A and n are constants. Specifically, for SS316L, the two constants are: $A = 50\mu m(k\ /s)\ and\ n = 0.4$ [152]. For the downskin region, the calculated cooling rate using the SDAS value is 1.81×10^4 k/sec, matching the value obtained using the PDAS.

Support structures typically provide an escape path in which heat is dissipated, however, with the downskin surface resting on loose powder during the printing process, the heat dissipation is significantly reduced. The thermal conductivity (λ) for SS316L at 1000°C bulk is reported to be approximately 3.5 times larger than that of the powder ($\lambda_{solid/bulk} \approx 26$ W m^{-1} $°C^{-1}$, $\lambda_{powder} \approx 8$ W m^{-1} $°C^{-1}$) [46, 153, 154], resulting in slower cooling and enlarged meltpool formation. In the vertical and upskin locations (Figure 14(a, b and c)), heat extraction through the bulk results in faster cooling rates, fostering the development of the observed small cell structure.

4.1.1.2 Solidification Front Velocity and Microsegregation Analysis

The analysis will be firstly presented on the bulk section. Based on the meltpool size measured at 112 μm (lateral diameter), the thermal gradient was calculated using Equation (4):

$$\mathcal{G} = \frac{\Delta T}{x} \qquad \text{(Eq.4)}$$

where G is the thermal gradient, ΔT is the temperature difference between the center and edge of the meltpool ($\Delta T = T_{boiling} - T_{liquidus} = 1400K$), and *x* is the meltpool lateral length. Therefore, the G value of the inner/outer/upskin locations are 1.25×10^7 K/m.

Figure 20 presents the KGT model curve, plotting the primary dendrite cell size as a function of the SFV for the SS316L composition used in this study at a G value of 1.25×10^7 K/m. Using the cell size and the KGT curve, the SFV is found to be 0.13 m/s.

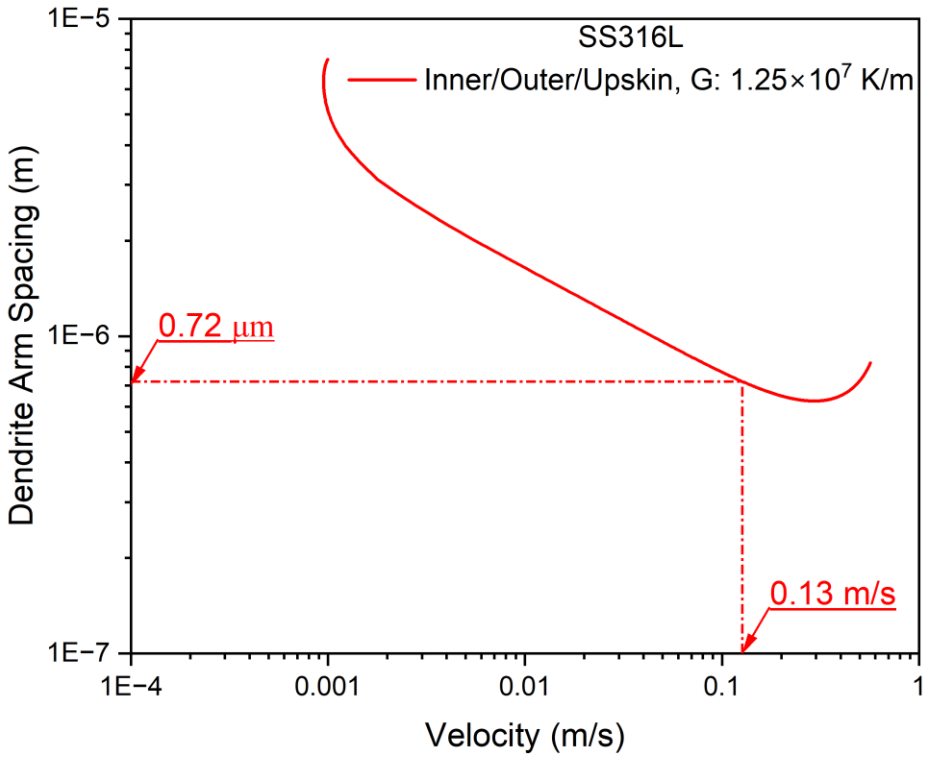

Figure 20. The KGT model for the LPBF SS316L composition used in this study with a G value of 1.2×10^7 k/m. (Note: the KGT curve is obtained by fitting a mathematical function based on present material properties and microstructural features.)

A microsegregation analysis was conducted to understand if the difference in solidification environment could play a role in the partitioning of the alloying element during solidification. Figure 21 presents the multicomponent relationship between the effective partition coefficient (K(v)) and SFV according to the continuous growth model from Aziz et al. [155]. The figure is plotted for the SS316L composition reported in Table 3, and for the inner/outer/upskin locations, a G value of 1.25×10^7 k/m is used. Using the SFV value obtained in Figure 20, the effective partition coefficient can be obtained. From Figure 21, negligible deviations between the effective partition coefficient in the current and equilibrium state is observed (ex: $Cr_{equilibrium}$: 0.790, Cr_{bulk}: 0.808), suggesting no significant change in microsegregation behavior is expected. Further, the downskin location experiences solidification conditions even closer to equilibrium compared to

bulk locations (i.e.; lower cooling rate, equiaxed microstructure), therefore, given the absence of significant levels of microsegregation in bulk locations, it is reasonable to infer a similar behavior in the downskin location. A study conducted by Qiu et al. [156] investigated the microstructure and tensile behaviour of LPBF SS316L concluded that no significant levels of microsegregation is observed in the matrix of the material at cooling rates $>10^6$ $℃/s$ due to the increase in partitioning coefficient and possibility of solute trapping effect. The results are also suggesting that the oxidation study should not be influenced by local changes in chemical composition originating from the rapid solidification experienced during printing.

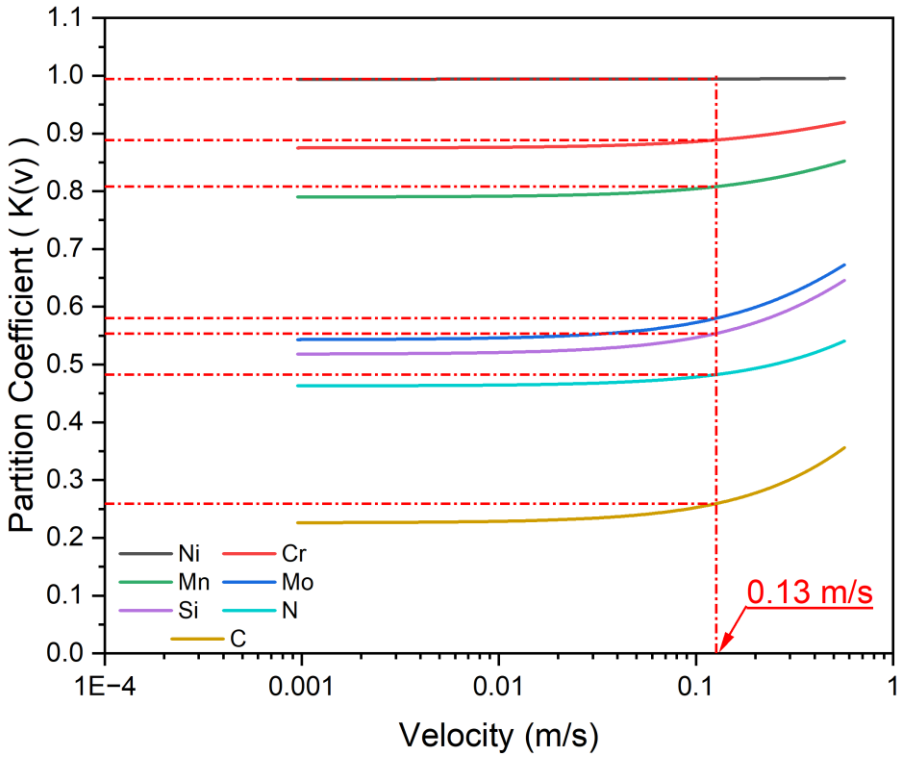

Figure 21. The multicomponent Aziz model for SS316L used in this study for G value of 1.2 × 10^7 k/m. (Note: the plotted curve is obtained by solving the Aziz model based on present material properties and microstructural features.)

4.1.1.3 Electron Backscatter Diffraction Analysis

As presented in Figure 13, the MUD values are below 3.28 for all four surfaces. Leicht et al. [70] investigated the effect of the 90, 45 and 67° scan rotations on the developed microstructure of LPBF SS316L parts. Leicht et al. concluded that parts produced using the 67° scan strategy yielded the weakest texture. Similarly in the present case, it can be concluded that all four studied locations do not exhibit any preferential texture orientation. Figure 22 presents the columnar to equiaxed transition (CET) diagram for LPBF SS316L, plotting the bulk (red) and downskin (blue) locations.

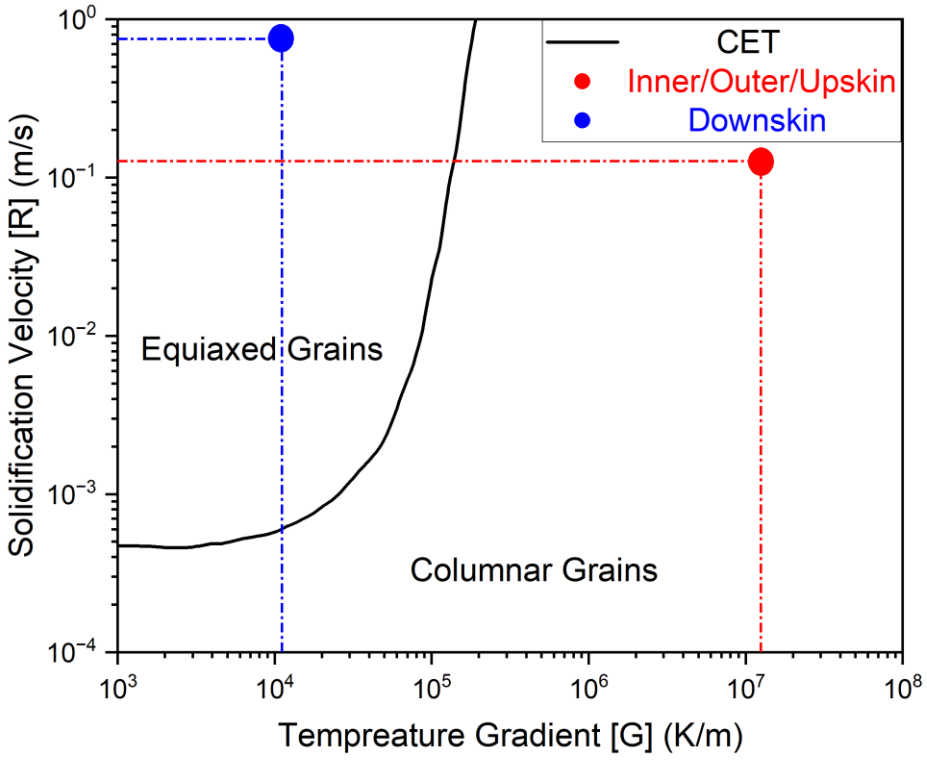

Figure 22. CET diagram for LPBF AM SS316 plotting the Bulk (Inner/Outer/Upskin) and Downskin locations. (Note: The CET transition curve was adapted from [157])

As discussed previously, during the LPBF process, the directionally prevalent heat transfers from the meltpool to the building substrate, leading to thermal gradients parallel to the building

directions, promotes the development of columnar grains in the building direction [70]. However, due to the scanning strategy during the build of the present samples (with 67° scan rotation), it takes more than four layers until the scan vector is in the same direction again (compared to two layers with 90° and four with 45° scan rotation), therefore, no clear sign of dominant columnar grains is observed in Figure 13. The 67° scan rotation has been previously shown to be the optimum scanning rotation to minimize the development of a columnar texture due to the favoured grain growth [43, 70]. Ultimately, as shown in Figure 14, the bulk region in theory develops a columnar texture, however, due to the utilized scanning strategy the columnar texture is therefore inhibited (Figure 13(a, b and c)). In addition, with regards to the downskin location, the EBSD crystallographic map (Figure 13(d)) presents an equiaxed texture which is further confirmed in the CET diagram presented (Figure 22).

4.1.2 Heat Treated Condition

With the utilized heat treatment temperature, 1050°C, recrystallization is induced leading to the coarser microstructure depicted in Figure 14.

Kong et al. [28] explored the effect of heat treatment at 1050°C for 0.5, 1 and 2 hour soaking time on LPBF 316L where the reported gain size after the HT was 35, 44 and 49 μm, respectively. The measured grain size at the bulk (90° inner, 90°outer and 0° upskin) sections in the present study fall within the reported range.

Figure 23 presents the combined measured microhardness - grain size data points against a similar plot reported by Yan et al. [32]. Ultimately, the obtained microhardness values in the present study fall within the range reported in the literature, between 165 to 198 HV [32]. Ultimately, the

presented values follow the Hall-Patch relationship, decreasing microhardness as the grain size is increased.

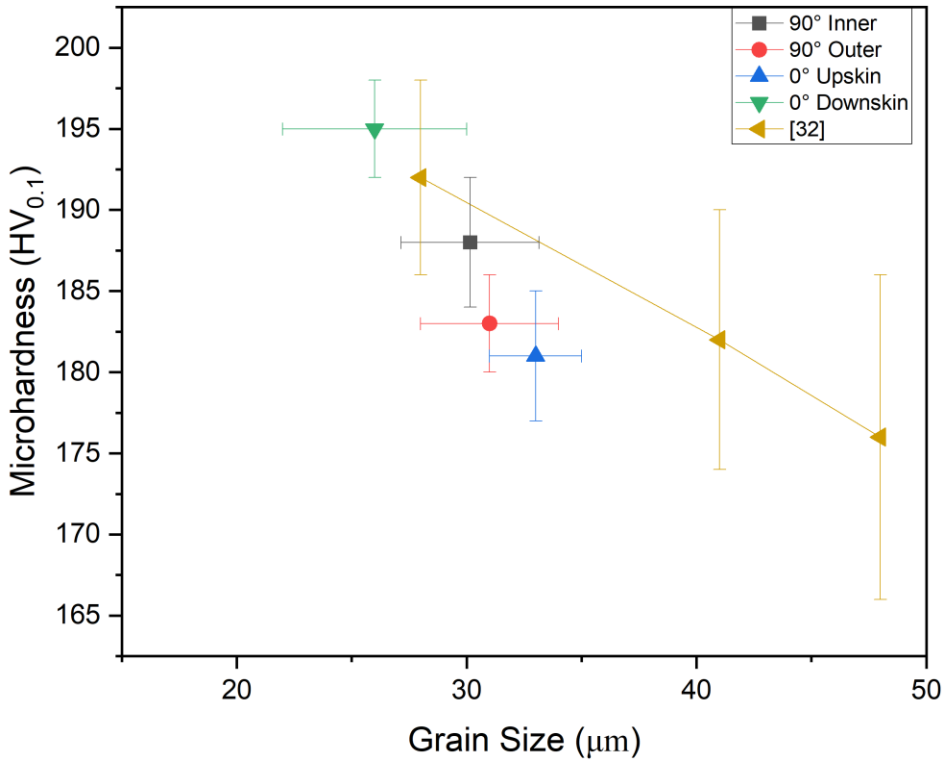

Figure 23. Microhardness as a function of the grain size for the HT surfaces. Values from literature are plotted for comparisons.

A similar trend of decreasing microhardness values post heat-treatment has been observed and reported by Wang et al. [116]. In addition, Zhou et al. [110] observed that the mechanical properties of AM SS316L are improved after subcritical temperature heat treatment (950°C) compared to the temperature range at which recrystallization occurs (1000-1200°C). The improvement is attributed to the elimination of melt pool boundaries and high-density dislocations while retaining the benefits of nano-inclusions and cellular substrates during subcritical heat treatment. Conversely, heat treatments within the recrystallization temperature range eliminated the cellular structure and reduced low-angle grain boundary density, leading to an increased oxidation rate and decreased

mechanical properties [110]. These findings are in alignment with the results observed in the present study.

4.1.2.1 Electron Backscatter Diffraction Analysis

With respect to the 0° downskin location, after the applied heat treatment, the three regions identified in Figure 13(d) are observed to transform into two regions in Figure 15(d). The transition region in the AB state appears to have transformed into one with equiaxed texture with larger grains compared to the downskin region. In addition, an observation can be made using the measured grain size reported in table 5 and Figure 15(d). In a uniform microstructure material, the effect of a heat treatment is uniform across [158], however, this is not the case as the initial cell size observed in the AB downskin location is larger than that of the vertical and upskin locations. While post heat treatment, the grain size at the downskin appears to be smaller than that of the vertical and upskin locations, suggesting that the grain growth rate observed at the downskin is slower than that of the vertical and upskin locations.

4.2 AB vs. HT Oxidation Response

The T0 sample presented in Figure 16 presents the lack of change in the microstructure during the heat cycle applied. Dudzik et al. [159] reported a similar lack of recrystallisation and remnants of the solidification structure and melt pool boundaries after 100 hrs. at 900°C. This confirmation allows us to assume unchanged AB and HT microstructure at the start of the applied oxidation cycle discussed in this section.

4.2.1 Chemical Analysis: XRD & EDS

The XRD spectra presented in Figure 17 concurs with the results of several studies on the oxides formed on LPBF SS316L in dry air atmosphere at 900°C; With the oxides being: Fe_2O_3 , Cr_2O_3 ,Cr_2FeO_4 and Cr_2MnO_4 oxides [22, 39, 40, 124, 159].

In addition, the EDS analysis presented in Figure 18 highlights the distribution of the formed oxides. Where a two-layer oxide evolution is observed to make up the majority of the oxide scale. As discussed earlier, the inner and outer layer are recognized as Cr2O3 and Fe2O3 oxides.

A two-layer oxide scale has been documented in several studies investigating the oxidation behaviour of LPBF SS316L components [22, 39, 40, 119, 147, 160]. The formation of this two-layer oxide scale is attributed to the presence of Cr, which is fast to react with oxygen gas in the oxidative environment due to its lower Gibbs free energy, forming the initial oxide layer [22, 161-163]. Following, it is reported in literature that the formation of the Fe_2O_3 oxide nucleates and grows on the outer surface of the Cr_2O_3 oxide, forming the second layer [22, 40, 162, 164]. Ultimately, the Cr2O3 oxide layer forms due to a chemical-based reaction while the Fe2O3 oxide follows diffusion (the diffusion of Fe through Cr2O3), therefore yielding an overall smaller oxide

scale. A study by Riffard et al. [165] established a timeline regarding the formation of different oxides on AISI 304 stainless steel at 1000°C dry air environment. The results show the formation of Cr_2O_3 during the first hour of oxidation, where the formation of Fe_2O_3 is only observed between after the 8-hour mark.

Further, for all samples, the formation of the Cr_2MnO_4 is observed as a thin layer slightly above the Cr_2O_3 oxide layer due to the faster diffusion of Mn than that of Cr through the chromia layer [159, 164]. Indeed, Lobnig et al. [164] reported that Mn diffuses through the chromia layer faster than Cr by two orders of magnitude (D_{Cr}: 3.3×10^{-17} m^2s^{-1}, D_{Mn}: 2.8×10^{-15} m^2s^{-1} [166]). Sabioni et al. [167] showed that due to Mn high affinity for oxygen (compared to Cr), Mn ions diffuse towards the outer surface, at which they react with Cr ions, creating Cr_2MnO_4 oxide. In addition, the Cr_2MnO_4 has a higher charge (+1, p-type), Cr_2O_3 (0), allowing it to form closer to the surface. In addition, Riffard et al. [165] also shows the formation Cr-Mn oxides during the first hour of oxidation at 1000°C dry air environment.

Further, several studies have linked grain boundaries to accelerated elemental diffusion short-paths due to atomic mismatch [22, 156, 159, 164, 168, 169]. This behavior, in oxidative environment, leads to rapid inward diffusion of oxygen into the sample. Therefore, the oxygen penetration depth into the material matrix was measured. Table 8 illustrates the measured oxygen penetration depth into the material matrix at the four AB and HT locations. The one-way ANOVA test suggests that for a $p<0.05$, the oxidation penetration depths are statistically equivalent regardless of the location (vertical vs horizontal).

Table 8. Oxygen penetration into the matrix at the four HT surfaces.

Location	Surface	Oxygen penetration depth (µm)	
		AB	HT
90° wall	Inner	5.8 ± 2.2	6.5 ± 1.8
	Outer	6.7 ± 2.7	7.0 ± 1.7
0° location	Upskin	6.3 ± 2.4	6.9 ± 2.0
	Downskin	7.2 ± 2.8	5.4 ± 1.3

The EDS maps of Figure 18 are suggesting the formation of silica (SiO_2) along the grain boundaries. Previous studies have show that grain boundaries provide paths for outward (Cr and Si) and inward (O) diffusion of elements [160, 170-174]. The low Gibbs free energy of formation of SiO_2 explain the internal oxidation. Several studies in literature have reported the formation of the observed Si oxide occur during the initial oxidation phase, progressing until the development of a uniform chromia oxide scale that constrains the inward diffusion of oxygen [160, 170-174]. A study by Taylor et al. [173] reported the importance of the formation of silica oxide on enhancing oxidation resistance in austenitic steel through a p-type oxidation mechanism. The authors have shown that after an extended oxidation period (400 hrs.), the formation of silica oxide occurs to an extent where grains at the surface of the material are encapsulated by the silicon oxide formed along the grain boundaries, thus acting as a diffusion barrier to the inner grain [173]. The formation of silica oxide could promote the early nucleation of Cr_2O_3, accelerating the establishment of this highly protective oxide layer [160, 171, 172]. In fact, Lobb at al. [170] showed that the addition of approximately 0.7% Si reduced the growth kinetics of Cr_2O_3 from $11 \times 10{-}5\ g^2.\ m{-}4.s^{-1}$ (0% Si) to $3 \times 10^{-5}\ g^2.\ m{-}4.s^{-1}$ at 900°C in high chromium steel. This behaviour resulted in the final chromia oxide layer to be 2.3 ± 0.5 instead of 5.4 ± 0.6 µm. Nonetheless, in the present study, due to the shorter oxidation cycle, the encapsulation of full grains is not observed.

4.2.2 Oxide Scale Thickness

Figure 24 summarises the measured oxide scale thickness along with a comparison of data from the literature [22, 159, 175], it presents the relationship between the oxidative environment temperature and the thickness of the developed oxide scale after 100hrs. The measured oxide thickness at the four locations falls within the reported range for AB LPBF SS316 oxidized at 900°C for 100 hrs., which ranges between 1 and 4 μm [22, 159].

To compare the current oxidation response, data points from Siri et al. [22], Fujikawa et al. [175] and Dudziak et al. [159] have been integrated. A trend can be observed from the results reported by authors, where the oxide scale thickness increases with the temperature increase.

It should be mentioned that due to the lack of reporting on heat treated LPBF SS316L oxidation performance, heat treated wrought SS316L data points are used. Nevertheless, the grain size reported for the wrought samples ranged between 30 and 60 μm. Where as the measured oxide thickness observed at the four locations falls within the range reported in the literature, between 3.5 and 11 μm [22, 159, 175].

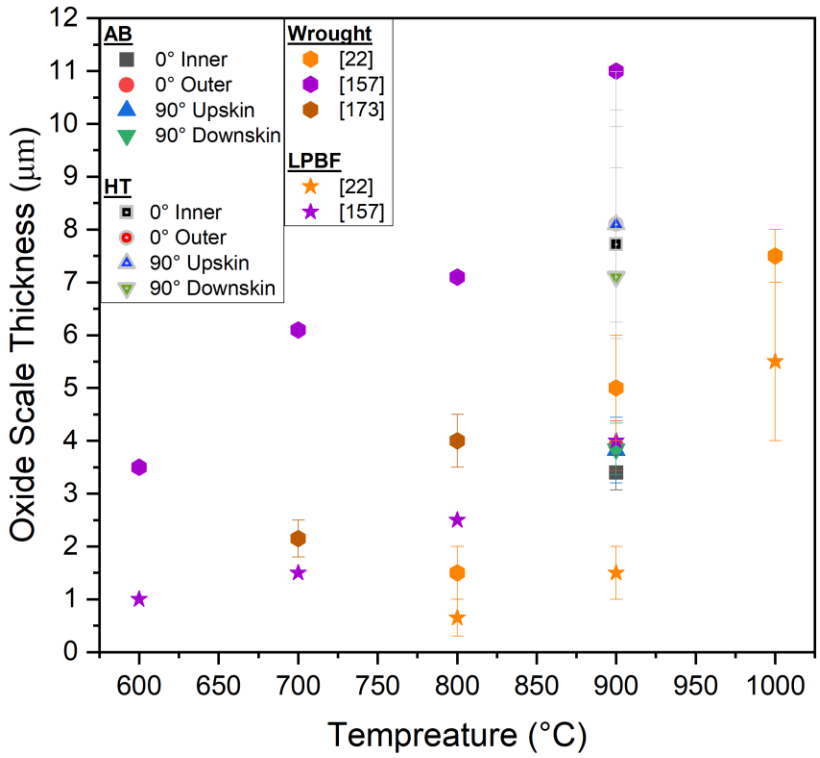

Figure 24. Oxide scale thickness as a function of temperature at the four AB and HT locations. Values from literature are plotted for comparisons.

Although the oxide scale composition in the HT condition seems to match that of the AB state, the HT part has a double oxide scale thickness, independently on the locations. The observed thickening of the oxide scale matches the literature that indicated that the applied HT exacerbates the oxidation resistance of LPBF AM SS316L [110]. Bedmar et al. [124] showed that after conducting a heat treatment at 1100°C, the developed scale thickness roughly doubled, increasing from 1.9 to 4.7 µm. Fujikawa et al. [175] showed that in wrought SS316, increasing the grain size by an order of magnitude approximately doubles the formed oxide scale thickness. The authors further explained the relationship between the microstructure and resultant oxide layer thickness through the diffusion of Cr. The flux ratio of Cr from grain boundary and internal diffusion is reported to exponentially decreases until the grain size reaches 10 µm, after which the effect of grain size on the flux ratio is less pronounced [175]. , therefore, the grain boundary density is

shown to have a positive correlation with Cr flux ratio. This is observed in the present study, where the sub-grain cellular structure of the AB condition (i.e. high boundary density) fosters a higher Cr flux towards the surface. On the other hand, after the heat treatment, the induced recrystallization and grain growth (i.e. low boundary density) reduces the AB Cr flux ratio, thus resulting in larger oxide layer thickness. In the present study, the grain size at the bulk of the AB and HT samples on average is 11.5 and 30 µm, respectively. While the oxide scale thickness of the AB and HT samples are 3.7 and 7.7 µm, respectively. Similar correlation between the grain size presented in the matrix and the developed oxide scale has been reported by Samal et al. [176], reporting smaller oxide scale with a smaller grain size due to smaller boundary surface area exposure. Trindade et al. [177] proposed that this behavior is attributed to the grain boundary diffusion mechanism, facilitating the transport of Cr toward the substrate/oxide interface. Therefore, small cell size (AB) stimulates faster Cr flux in contrast to larger grains (HT), accelerating the development of a continuous Cr_2O_3 layer. The decrease in the grain boundary density post heat treatment changes the oxidation mode from diffusion-driven to reaction-driven oxidation, resulting in an overall thicker oxide layer.

Chapter 5 Conclusions

The development of support-free LPBF printing protocols presents an opportunity to reduce the cost per part and waste material associated to the process. In the present study, an in-house developed support-free fabrication strategy via laser powder bed fusion is utilized to manufacture a SS316L support-free dome samples to study the effect of support-less printing on the microstructure, hardness and long-term oxidative behaviour of surfaces approaching zero-degree overhang. A heat treatment was applied to study its further effects.

Due to the supportless nature of the dome sample, low-angle overhang surfaces are seen to form a downskin, which is characterize by larger cell structure. In the AB state, the bulk microstructure presented similar to that reported in literature with primary dendritic arms spacing (PDAS) measuring 0.72 ± 0.09. However, due to the slower cooling rate at the downskin surface, PDAS and secondary dendritic arms (SDAS) are measured at 3.19 ± 0.20 and 0.99 ± 0.18 μm, respectively. Microhardness testing was conducted to evaluate the mechanical properties of the downskin with relation to the bulk. The microhardness values, following Hall-Patch equation, were 244 ± 5 and 225 ± 3 HV for the bulk and downskin surfaces, respectively. In addition, a microsegregation analysis was conducted to establish a proper understating of the matrix prior to heat treating and oxidizing the samples. The analysis showed no significant levels of microsegregation.

After a heat treatment at 1050°C for 1 hour, the grain size was observed to enlarge, measuring at 31 ± 3 and 26 ± 3 μm for the bulk and downskin surfaces, respectively. Nonetheless, the HT grain size at the downskin measured smaller than that of the bulk, suggesting a slower grain growth rate.

Thus, microhardness values are observed to drop after the heat treatment, with values of 184 ± 4 and 195 ± 3 HV for the bulk and downskin, respectively.

Finally, the oxidative behaviour of AB and HT samples at 900°C for 100 hours in dry air was tested, and the XRD results showed similar chemical composition of the oxide scale, forming Fe_2O_3 , Cr_2O_3 ,Cr_2FeO_4 and Cr_2MnO_4 oxides.

Although the AB bulk and downskin have presented a mismatch in the length scale of the microstructural features, the oxide scale thickness is measured at 3.7 ± 1.7 and 3.8 ± 1.8 μm at the bulk and downskin surfaces, respectively. While for the HT condition, due to the enlarged microstructure, the oxide scale thickness is larger than that of the AB state, measuring at 7.9 ± 2.4 and 7.1 ± 2.1 μm for the bulk and downskin surfaces, respectively.

Ultimately, in an effort to understand the effects of support-free printing of low-angle overhang surfaces on LPBF SS316L microstructure, mechanical and oxidative behaviour in AB and HT state. Therefor, manufacturing of support-free low-angle overhang LPBFSS316L results in:

1. Enlarged microstructure due to heat accumulation, typically dissipated by supports.
    a. Resulting in drop in mechanical properties, evaluated via microhardness testing.
2. Increased oxide scale thickness due to larger microstructural features.
3. Following heat treatment, recrystallization at the downskin surface was slower than in the bulk, resulting in smaller grain size and thinner oxide scale.
4. Post heat treatment, the oxide scale was generally thicker, correlating with larger grains structure.

The findings of this research allow us to take a step closer to understanding the nature of support-free LPBF manufacturing and its limitations.

Chapter 6 References

[1] A. Uriondo, M. Esperon-Miguez, and S. Perinpanayagam, "The present and future of additive manufacturing in the aerospace sector: A review of important aspects," *Proceedings of the Institution of Mechanical Engineers, Part G: Journal of Aerospace Engineering,* vol. 229, no. 11, pp. 2132-2147, 2015, doi: 10.1177/0954410014568797.

[2] J. C. Najmon, S. Raeisi, and A. Tovar, "Review of additive manufacturing technologies and applications in the aerospace industry," in *Additive Manufacturing for the Aerospace Industry*, 2019, pp. 7-31.

[3] B. Blakey-Milner *et al.*, "Metal additive manufacturing in aerospace: A review," *Materials & Design,* vol. 209, 2021, doi: 10.1016/j.matdes.2021.110008.

[4] C. Culmone, G. Smit, and P. Breedveld, "Additive manufacturing of medical instruments: A state-of-the-art review," *Additive Manufacturing,* vol. 27, pp. 461-473, 2019, doi: 10.1016/j.addma.2019.03.015.

[5] J. P. Oliveira, A. D. LaLonde, and J. Ma, "Processing parameters in laser powder bed fusion metal additive manufacturing," *Materials & Design,* vol. 193, 2020, doi: 10.1016/j.matdes.2020.108762.

[6] M. Salmi, "Additive Manufacturing Processes in Medical Applications," *Materials (Basel),* vol. 14, no. 1, Jan 3 2021, doi: 10.3390/ma14010191.

[7] A. Behjat *et al.*, "Enhanced surface properties and bioactivity of additively manufactured 316L stainless steel using different post-treatments," *Materials Today: Proceedings,* vol. 70, pp. 188-194, 2022, doi: 10.1016/j.matpr.2022.09.019.

[8] L. Y. K. H. B. Baughman, D. G. F. Medina, and M. M. S. Wiener, *Additive Manufacturing of Metals: The Technology, Materials, Design and Production*.

[9] E. Maleki, S. Bagherifard, M. Bandini, and M. Guagliano, "Surface post-treatments for metal additive manufacturing: Progress, challenges, and opportunities," *Additive Manufacturing,* vol. 37, 2021, doi: 10.1016/j.addma.2020.101619.

[10] R. Mertens, L. Baert, K. Vanmeensel, and B. Van Hooreweder, "Laser powder bed fusion of high strength aluminum," *Material Design & Processing Communications,* vol. 3, no. 5, 2020, doi: 10.1002/mdp2.161.

[11] Z. Xiao, W. Yu, H. Fu, Y. Deng, Y. Wu, and H. Zheng, "Recent progress on microstructure manipulation of aluminium alloys manufactured via laser powder bed fusion," *Virtual and Physical Prototyping,* vol. 18, no. 1, 2022, doi: 10.1080/17452759.2022.2125880.

[12] P. A. Rometsch, Y. Zhu, X. Wu, and A. Huang, "Review of high-strength aluminium alloys for additive manufacturing by laser powder bed fusion," *Materials & Design,* vol. 219, 2022, doi: 10.1016/j.matdes.2022.110779.

[13] S. Cao, Y. Zou, C. V. S. Lim, and X. Wu, "Review of laser powder bed fusion (LPBF) fabricated Ti-6Al-4V: process, post-process treatment, microstructure, and property," *Light: Advanced Manufacturing,* vol. 2, no. 2, 2021, doi: 10.37188/lam.2021.020.

[14] D. Simson and S. K. Subbu, "Effect of Process Parameters on Surface Integrity of LPBF Ti6Al4V," *Procedia CIRP,* vol. 108, pp. 716-721, 2022, doi: 10.1016/j.procir.2022.03.111.

[15] Z. Song, X. Zeng, and L. Wang, "Laser additive manufacturing of titanium alloys with various Al contents," *Materials Research Letters,* vol. 11, no. 5, pp. 391-398, 2023, doi: 10.1080/21663831.2023.2165418.

[16] Z. Tian *et al.*, "A Review on Laser Powder Bed Fusion of Inconel 625 Nickel-Based Alloy," *Applied Sciences,* vol. 10, no. 1, 2019, doi: 10.3390/app10010081.

[17] T. Huynh *et al.*, "Microstructural Development in Inconel 718 Nickel-Based Superalloy Additively Manufactured by Laser Powder Bed Fusion," *Metallography, Microstructure, and Analysis,* vol. 11, no. 1, pp. 88-107, 2022, doi: 10.1007/s13632-021-00811-0.

[18] W. Guo *et al.*, "Effect of laser scanning speed on the microstructure, phase transformation and mechanical property of NiTi alloys fabricated by LPBF," *Materials & Design,* vol. 215, 2022, doi: 10.1016/j.matdes.2022.110460.

[19] C. Guerra, J. A. Ramos-Grez, I. La Fé-Perdomo, A. Castillo, and M. Walczak, "Microstructure and Mechanical Properties of Cu-11Al-5Ni-4Fe wt% Manufactured by LPBF," *Metals,* vol. 13, no. 3, 2023, doi: 10.3390/met13030459.

[20] S. D. Jadhav, P. P. Dhekne, S. Dadbakhsh, J.-P. Kruth, J. Van Humbeeck, and K. Vanmeensel, "Surface Modified Copper Alloy Powder for Reliable Laser-based Additive Manufacturing," *Additive Manufacturing,* vol. 35, 2020, doi: 10.1016/j.addma.2020.101418.

[21] X. Yang, Y. Qi, W. Zhang, Y. Wang, and H. Zhu, "Laser powder bed fusion of C18150 copper alloy with excellent comprehensive properties," *Materials Science and Engineering: A,* vol. 862, 2023, doi: 10.1016/j.msea.2022.144512.

[22] C. Siri, I. Popa, A. Vion, C. Langlade, and S. Chevalier, "Impact of Selective Laser Melting Additive Manufacturing on the High Temperature Behavior of AISI 316L Austenitic Stainless Steel," *Oxidation of Metals,* vol. 94, no. 5-6, pp. 527-548, 2020, doi: 10.1007/s11085-020-10005-8.

[23] S. Tekumalla, B. Selvarajou, S. Raman, S. Gao, and M. Seita, "The role of the solidification structure on orientation-dependent hardness in stainless steel 316L produced by laser powder bed fusion," *Materials Science and Engineering: A,* vol. 833, 2022, doi: 10.1016/j.msea.2021.142493.

[24] H. Zhou *et al.*, "The microstructure and properties evolution of SS316L fabricated by magnetic field-assisted laser powder bed fusion," *Materials Science and Engineering: A,* vol. 845, 2022, doi: 10.1016/j.msea.2022.143216.

[25] A. Yadollahi, N. Shamsaei, S. M. Thompson, and D. W. Seely, "Effects of process time interval and heat treatment on the mechanical and microstructural properties of direct laser deposited 316L stainless steel," *Materials Science and Engineering: A,* vol. 644, pp. 171-183, 2015, doi: 10.1016/j.msea.2015.07.056.

[26] W. M. Tucho, V. H. Lysne, H. Austbø, A. Sjolyst-Kverneland, and V. Hansen, "Investigation of effects of process parameters on microstructure and hardness of SLM manufactured SS316L," *Journal of Alloys and Compounds,* vol. 740, pp. 910-925, 2018, doi: 10.1016/j.jallcom.2018.01.098.

[27] X. Wang, J. A. Muñiz-Lerma, O. Sánchez-Mata, M. Attarian Shandiz, and M. Brochu, "Microstructure and mechanical properties of stainless steel 316L vertical struts manufactured by laser powder bed fusion process," *Materials Science and Engineering: A,* vol. 736, pp. 27-40, 2018, doi: 10.1016/j.msea.2018.08.069.

[28] D. Kong *et al.*, "Mechanical properties and corrosion behavior of selective laser melted 316L stainless steel after different heat treatment processes," *Journal of Materials Science & Technology,* vol. 35, no. 7, pp. 1499-1507, 2019, doi: 10.1016/j.jmst.2019.03.003.

[29] M. Gor, H. Soni, G. Singh Rajput, and P. Sahlot, "Experimental investigation of mechanical properties for wrought and selective laser melting additively manufactured SS316L and MS300," *Materials Today: Proceedings,* vol. 62, pp. 7215-7219, 2022, doi: 10.1016/j.matpr.2022.03.511.

[30] E. Tascioglu, Y. Karabulut, and Y. Kaynak, "Influence of heat treatment temperature on the microstructural, mechanical, and wear behavior of 316L stainless steel fabricated by laser powder bed additive manufacturing," *The International Journal of Advanced Manufacturing Technology,* vol. 107, no. 5-6, pp. 1947-1956, 2020, doi: 10.1007/s00170-020-04972-0.

[31] W.-S. Shin *et al.*, "Heat treatment effect on the microstructure, mechanical properties, and wear behaviors of stainless steel 316L prepared via selective laser melting," *Materials Science and Engineering: A,* vol. 806, 2021, doi: 10.1016/j.msea.2021.140805.
[32] F. Yan, W. Xiong, E. Faierson, and G. B. Olson, "Characterization of nano-scale oxides in austenitic stainless steel processed by powder bed fusion," *Scripta Materialia,* vol. 155, pp. 104-108, 2018, doi: 10.1016/j.scriptamat.2018.06.011.
[33] A. L. Johnson *et al.*, "Spectroscopic and microscopic investigation of the corrosion of 316/316L stainless steel by lead–bismuth eutectic (LBE) at elevated temperatures: importance of surface preparation," *Journal of Nuclear Materials,* vol. 328, no. 2-3, pp. 88-96, 2004, doi: 10.1016/j.jnucmat.2004.03.006.
[34] J. Pitter, F. Cerny, J. Cizner, J. Suchanek, and D. Tischler, "High temperature corrosion properties of SiNx and CrNx coatings deposited by IBAD method," *Surface and Coatings Technology,* vol. 200, no. 1-4, pp. 73-76, 2005, doi: 10.1016/j.surfcoat.2005.02.059.
[35] A. A. Syed, A. Denoirjean, P. Fauchais, and J. C. Labbe, "On the oxidation of stainless steel particles in the plasma jet," *Surface and Coatings Technology,* vol. 200, no. 14-15, pp. 4368-4382, 2006, doi: 10.1016/j.surfcoat.2005.02.156.
[36] M.-Z. H. SEUNG-GOO KIM, SUNG PIL YOON, JONGHEE HAN, SUK WOO NAM, and T. H. L. A. S.-A. HONG, "Preparation of YSZ Coated AISI-Type 316L Stainless Steel by the Sol-Gel Coating Method and Its Corrosion Behavior in Molten Carbonate."
[37] J. L. S. J. E. Indacochea, K. R. Litko, E. J. Karell, and and A. G. Raraz, "High-Temperature Oxidation and Corrosion of Structural Materials in Molten Chlorides."
[38] A. Vesel, M. Mozetic, A. Drenik, N. Hauptman, and M. Balat-Pichelin, "High temperature oxidation of stainless steel AISI316L in air plasma," *Applied Surface Science,* vol. 255, no. 5, pp. 1759-1765, 2008, doi: 10.1016/j.apsusc.2008.06.017.
[39] Y.-J. Hwang, D.-Y. Wi, K.-S. Kim, and K.-A. Lee, "High Temperature Oxidation Behavior of 316L Austenitic Stainless Steel Manufactured by Laser Powder Bed Fusion Process," *Journal of Korean Powder Metallurgy Institute,* vol. 28, no. 2, pp. 110-119, 2021, doi: 10.4150/kpmi.2021.28.2.110.
[40] H. Wu, Z. Liang, Z. Zhu, B. Tang, and Q. Zhao, "Oxidation resistance of the 316L manufactured by cold-rolled and selective laser melting in CO2 and air," *Materials Today Communications,* vol. 33, 2022, doi: 10.1016/j.mtcomm.2022.104889.
[41] H. Buscail, S. El Messki, F. Riffard, S. Perrier, R. Cueff, and C. Issartel, "Role of molybdenum on the AISI 316L oxidation at 900 °C," *Journal of Materials Science,* vol. 43, no. 21, pp. 6960-6966, 2008, doi: 10.1007/s10853-008-2965-7.
[42] K. Bartsch and C. Emmelmann, "Enabling Cost-Based Support Structure Optimization in Laser Powder Bed Fusion of Metals," *Jom,* vol. 74, no. 3, pp. 1126-1135, 2021, doi: 10.1007/s11837-021-05055-5.
[43] A. Kumar, M. A. Shandiz, F. Sikan, and M. Brochu, "Microstructural and mechanical properties of an internal support-free IN625 closed impeller manufactured via laser powder bed fusion (L-PBF)," *Materials Science and Engineering: A,* vol. 874, 2023, doi: 10.1016/j.msea.2023.145080.
[44] V. Viale, J. Stavridis, A. Salmi, F. Bondioli, and A. Saboori, "Optimisation of downskin parameters to produce metallic parts via laser powder bed fusion process: an overview," *The International Journal of Advanced Manufacturing Technology,* vol. 123, no. 7-8, pp. 2159-2182, 2022, doi: 10.1007/s00170-022-10314-z.
[45] D. Herzog *et al.*, "Design guidelines for laser powder bed fusion in Inconel 718," *Journal of Laser Applications,* vol. 34, no. 1, 2022, doi: 10.2351/7.0000508.

[46] G. Piscopo, A. Salmi, and E. Atzeni, "On the quality of unsupported overhangs produced by laser powder bed fusion," *International Journal of Manufacturing Research,* vol. 14, no. 2, pp. 198-216, 2019, doi: http://dx.doi.org/10.1504/IJMR.2020.10019045.
[47] H. Paris, H. Mokhtarian, E. Coatanéa, M. Museau, and I. F. Ituarte, "Comparative environmental impacts of additive and subtractive manufacturing technologies," *CIRP Annals,* vol. 65, no. 1, pp. 29-32, 2016, doi: 10.1016/j.cirp.2016.04.036.
[48] J. V. K. Tanisha Pereira, Johan Potgieter, "A comparison of traditional manufacturing vs additive manufacturing, the best method for the job," *Procedia Manufacturing,* vol. 30, pp. 11-18, 2019, doi: https://doi.org/10.1016/j.promfg.2019.02.003.
[49] O. N. R. Kobryn P.A. , "Additive Manufacturing of Aerospace Alloys for Aircraft Structures," in *Cost Effective Manufacture via Net-Shape processing*, 2006. [Online]. Available: http://www.rto.nato.int/abstracts.asp. [Online]. Available: http://www.rto.nato.int/abstracts.asp
[50] B. C. Gross, J. L. Erkal, S. Y. Lockwood, C. Chen, and D. M. Spence, "Evaluation of 3D printing and its potential impact on biotechnology and the chemical sciences," *Anal Chem,* vol. 86, no. 7, pp. 3240-53, Apr 1 2014, doi: 10.1021/ac403397r.
[51] R. Kumar, M. Kumar, and J. S. Chohan, "The role of additive manufacturing for biomedical applications: A critical review," *Journal of Manufacturing Processes,* vol. 64, pp. 828-850, 2021, doi: 10.1016/j.jmapro.2021.02.022.
[52] Z. Hasan, "Future lookout," in *Tooling for Composite Aerospace Structures*, 2020, pp. 231-240.
[53] N. Chekir, "Laser wire deposition additive manufacturing of Ti-6Al-4V for the aerospace industry," *McGill University Libraries,* 2019. [Online]. Available: https://library-archives.canada.ca/eng/services/services-libraries/theses/Pages/item.aspx?idNumber=1117447209.
[54] G. Profozich, "Top 8 Industries Benefiting from Additive Manufacturing," 24/07/2024 2021. [Online]. Available: https://www.cmtc.com/blog/six-industries-benefiting-from-additive-manufacturing.
[55] J. V. H. G. V. Petrovic, O. Jordá Ferrando, J. Delgado Gordillo, J. Ramón and a. L. P. G. Blasco Puchades, "Additive layered manufacturing: sectors of

industrial application shown through case studies," *International Journal of Production*

Research, vol. 49, pp. 1061-1079, 2011.
[56] S. H. Huang, P. Liu, A. Mokasdar, and L. Hou, "Additive manufacturing and its societal impact: a literature review," *The International Journal of Advanced Manufacturing Technology,* vol. 67, no. 5-8, pp. 1191-1203, 2012, doi: 10.1007/s00170-012-4558-5.
[57] A. R. Andrea Soffietti , Mattia Scarinzi , Pradeep Kumar , and Ritik Raghvendra Shukla "Additive Manufacturing in the watch industry," 2022.
[58] M. Dadkhah, J.-M. Tulliani, A. Saboori, and L. Iuliano, "Additive manufacturing of ceramics: Advances, challenges, and outlook," *Journal of the European Ceramic Society,* vol. 43, no. 15, pp. 6635-6664, 2023, doi: 10.1016/j.jeurceramsoc.2023.07.033.
[59] H. P. Van-Thao Le, Guillaume Mandil, "Using additive and subtractive manufacturing

technologies in a new remanufacturing strategy to

produce new parts from End-of-Life parts," in *Congrès Français de Mécanique* Lyon, 2015: HAL
[60] K. Kanishka and B. Acherjee, "Revolutionizing manufacturing: A comprehensive overview of additive manufacturing processes, materials, developments, and challenges," *Journal of Manufacturing Processes,* vol. 107, pp. 574-619, 2023, doi: 10.1016/j.jmapro.2023.10.024.

[61] P. Lakkala, S. R. Munnangi, S. Bandari, and M. Repka, "Additive manufacturing technologies with emphasis on stereolithography 3D printing in pharmaceutical and medical applications: A review," *Int J Pharm X,* vol. 5, p. 100159, Dec 2023, doi: 10.1016/j.ijpx.2023.100159.
[62] M. Hoffmann and A. Elwany, "In-Space Additive Manufacturing: A Review," *Journal of Manufacturing Science and Engineering,* vol. 145, no. 2, 2023, doi: 10.1115/1.4055603.
[63] N. A. Charoo *et al.*, "Selective laser sintering 3D printing - an overview of the technology and pharmaceutical applications," *Drug Dev Ind Pharm,* vol. 46, no. 6, pp. 869-877, Jun 2020, doi: 10.1080/03639045.2020.1764027.
[64] Y. Yan *et al.*, "Progress and opportunities in additive manufacturing of electrically conductive polymer composites," *Materials Today Advances,* vol. 17, 2023, doi: 10.1016/j.mtadv.2022.100333.
[65] S. Traore *et al.*, "Influence of gas atmosphere (Ar or He) on the laser powder bed fusion of a Ni-based alloy," *Journal of Materials Processing Technology,* vol. 288, 2021, doi: 10.1016/j.jmatprotec.2020.116851.
[66] P. V. Cobbinah, R. A. Nzeukou, O. T. Onawale, and W. R. Matizamhuka, "Laser Powder Bed Fusion of Potential Superalloys: A Review," *Metals,* vol. 11, no. 1, 2020, doi: 10.3390/met11010058.
[67] L. Thijs, F. Verhaeghe, T. Craeghs, J. V. Humbeeck, and J.-P. Kruth, "A study of the microstructural evolution during selective laser melting of Ti–6Al–4V," *Acta Materialia,* vol. 58, no. 9, pp. 3303-3312, 2010, doi: 10.1016/j.actamat.2010.02.004.
[68] E. P. Su W-N , Dickens P M, "Investigation of fully dense laser sintering of tool steel powder using a pulsed Nd:YAG (neodymium-doped yttrium aluminium garnet) laser," *Mechanical Engineering Science,* vol. 217, C, pp. 127 - 138, 2003, doi: https://doi.org/10.1243/095440603762554677.
[69] D. K. W. Dewidar M M , Wright C S, "Processing conditions and mechanical properties of high-speed steel parts fabricated using direct selective laser sintering," *Engineering Manufacture,* vol. 217, B, pp. 1651 -1663, 2003, doi: https://doi.org/10.1243/095440503772680587.
[70] A. Leicht, C. H. Yu, V. Luzin, U. Klement, and E. Hryha, "Effect of scan rotation on the microstructure development and mechanical properties of 316L parts produced by laser powder bed fusion," *Materials Characterization,* vol. 163, 2020, doi: 10.1016/j.matchar.2020.110309.
[71] Y. Wang *et al.*, "Microstructures and properties of equimolar AlCoCrCuFeNi high-entropy alloy additively manufactured by selective laser melting," *Intermetallics,* vol. 120, 2020, doi: 10.1016/j.intermet.2020.106746.
[72] S. Luo, P. Gao, H. Yu, J. Yang, Z. Wang, and X. Zeng, "Selective laser melting of an equiatomic AlCrCuFeNi high-entropy alloy: Processability, non-equilibrium microstructure and mechanical behavior," *Journal of Alloys and Compounds,* vol. 771, pp. 387-397, 2019, doi: 10.1016/j.jallcom.2018.08.290.
[73] Y.-K. Kim, J. Choe, and K.-A. Lee, "Selective laser melted equiatomic CoCrFeMnNi high-entropy alloy: Microstructure, anisotropic mechanical response, and multiple strengthening mechanism," *Journal of Alloys and Compounds,* vol. 805, pp. 680-691, 2019, doi: 10.1016/j.jallcom.2019.07.106.
[74] J. P. Kruth, L. Froyen, J. Van Vaerenbergh, P. Mercelis, M. Rombouts, and B. Lauwers, "Selective laser melting of iron-based powder," *Journal of Materials Processing Technology,* vol. 149, no. 1-3, pp. 616-622, 2004, doi: 10.1016/j.jmatprotec.2003.11.051.
[75] E. Yasa, Deckers, J. and Kruth, J., "The investigation of the influence of laser re-melting on density, surface quality and microstructure of selective laser melting parts," *Rapid Prototyping Journal,* vol. 17, pp. 312 - 327, 2011, doi: https://doi.org/10.1108/13552541111156450.

[76] A. Lamikiz, J. A. Sánchez, L. N. López de Lacalle, and J. L. Arana, "Laser polishing of parts built up by selective laser sintering," *International Journal of Machine Tools and Manufacture,* vol. 47, no. 12-13, pp. 2040-2050, 2007, doi: 10.1016/j.ijmachtools.2007.01.013.

[77] N. Kang, Y. Fu, P. Coddet, B. Guelorget, H. Liao, and C. Coddet, "On the microstructure, hardness and wear behavior of Al-Fe-Cr quasicrystal reinforced Al matrix composite prepared by selective laser melting," *Materials & Design,* vol. 132, pp. 105-111, 2017, doi: 10.1016/j.matdes.2017.06.060.

[78] A. J. P. MORGAN R. H, C. SUTCLIFFE, P. FOX, W. O'NEILL, "High density net shape components by direct laser re-melting of single-phase powders," *JOURNAL OF MATERIALS SCIENCE* vol. 37, pp. 3093 - 3100, 2002, doi: https://doi.org/10.1023/A:1016185606642.

[79] H. C. Hyer and C. M. Petrie, "Effect of powder layer thickness on the microstructural development of additively manufactured SS316," *Journal of Manufacturing Processes,* vol. 76, pp. 666-674, 2022, doi: 10.1016/j.jmapro.2022.02.047.

[80] G. V. de Leon Nope, L. I. Perez-Andrade, J. Corona-Castuera, D. G. Espinosa-Arbelaez, J. Muñoz-Saldaña, and J. M. Alvarado-Orozco, "Study of volumetric energy density limitations on the IN718 mesostructure and microstructure in laser powder bed fusion process," *Journal of Manufacturing Processes,* vol. 64, pp. 1261-1272, 2021, doi: 10.1016/j.jmapro.2021.02.043.

[81] E. O. Olakanmi, R. F. Cochrane, and K. W. Dalgarno, "A review on selective laser sintering/melting (SLS/SLM) of aluminium alloy powders: Processing, microstructure, and properties," *Progress in Materials Science,* vol. 74, pp. 401-477, 2015, doi: 10.1016/j.pmatsci.2015.03.002.

[82] E. O. Olakanmi, R. F. Cochrane, and K. W. Dalgarno, "Densification mechanism and microstructural evolution in selective laser sintering of Al–12Si powders," *Journal of Materials Processing Technology,* vol. 211, no. 1, pp. 113-121, 2011, doi: 10.1016/j.jmatprotec.2010.09.003.

[83] R. Li, J. Liu, Y. Shi, L. Wang, and W. Jiang, "Balling behavior of stainless steel and nickel powder during selective laser melting process," *The International Journal of Advanced Manufacturing Technology,* vol. 59, no. 9-12, pp. 1025-1035, 2011, doi: 10.1007/s00170-011-3566-1.

[84] C. U. Brown *et al.*, "The Effects of Laser Powder Bed Fusion Process Parameters on Material Hardness and Density for Nickel Alloy 625," *NIST Advanced Manufacturing Series,* vol. 100-19, 2018, doi: https://doi.org/10.6028/NIST.AMS.100-19.

[85] W. Yuan, H. Chen, T. Cheng, and Q. Wei, "Effects of laser scanning speeds on different states of the molten pool during selective laser melting: Simulation and experiment," *Materials & Design,* vol. 189, 2020, doi: 10.1016/j.matdes.2020.108542.

[86] J. Guzmán *et al.*, "Laser powder bed fusion parameters to produce high-density Ti–53%Nb alloy using irregularly shaped powder from hydride-dehydride (HDH) process," *Journal of Materials Research and Technology,* vol. 10, pp. 1372-1381, 2021, doi: 10.1016/j.jmrt.2020.12.084.

[87] M. R. Jandaghi, H. Pouraliakbar, L. Iannucci, V. Fallah, and M. Pavese, "Comparative assessment of gas and water atomized powders for additive manufacturing of 316 L stainless steel: Microstructure, mechanical properties, and corrosion resistance," *Materials Characterization,* vol. 204, 2023, doi: 10.1016/j.matchar.2023.113204.

[88] T. DebRoy *et al.*, "Additive manufacturing of metallic components – Process, structure and properties," *Progress in Materials Science,* vol. 92, pp. 112-224, 2018, doi: 10.1016/j.pmatsci.2017.10.001.

[89] W. J. Sames, F. A. List, S. Pannala, R. R. Dehoff, and S. S. Babu, "The metallurgy and processing science of metal additive manufacturing," *International Materials Reviews,* vol. 61, no. 5, pp. 315-360, 2016, doi: 10.1080/09506608.2015.1116649.

[90] E. C. Tomasz Kurzynowski, Bogumiła Kuźnicka, Jacek Reiner "Parameters in selective laser melting for processing metallic powders," *High Power Laser Materials Processing: Lasers, Beam Delivery, Diagnostics, and Applications,* 2012, doi: https://doi.org/10.1117/12.907292.
[91] I. Yadroitsev, A. Gusarov, I. Yadroitsava, and I. Smurov, "Single track formation in selective laser melting of metal powders," *Journal of Materials Processing Technology,* vol. 210, no. 12, pp. 1624-1631, 2010, doi: 10.1016/j.jmatprotec.2010.05.010.
[92] R. M. German, "Particle packing characteristics," *Metal Powder Industries Federation,* 1989.
[93] Y. V. K. Nikolay K. Tolochko, Sergei E. Mozzharov, Michail B. Ignatiev, Tahar Laoui, Victor I. Titov, "Absorptance of powder materials suitable for laser sintering," *Rapid Prototyping Journal,* vol. 6, pp. 155 - 161, 2000, doi: https://doi.org/10.1108/13552540010337029.
[94] N. Ulf. "D90, D50, D10, and span – for DLS?" https://www.malvernpanalytical.com/en/learn/knowledge-center/insights/d90-d50-d10-and-span-for-dls (accessed.
[95] R. N. Lumley, , and G. B. Schaffer, "THE EFFECT OF SOLUBILITY AND PARTICLE SIZE

ON LIQUID PHASE SINTERING " *Scripta Materialia,* vol. 35, no. 5, pp. 589 - 595, 1996, doi: https://doi.org/10.1016/1359-6462(96)00195-9.
[96] A. B. Spierings, N. H. , and G. L. , "Influence of the particle size distribution on surface quality and mechanical properties in

additive manufactured stainless steel parts," *Rapid Prototyping Journal,* vol. 17, no. 3, 2011, doi: http://dx.doi.org/10.1108/13552541111124770.
[97] K. W. D. M M Dewidar, and C S WrightView all authors and affiliations, "Processing conditions and mechanical properties of high-speed steel parts fabricated using direct selective laser sintering," *Journal of Engineering Manufacture,* vol. 217, no. 12, 2003, doi: https://doi.org/10.1243/095440503772680587.
[98] W. Abd-Elaziem *et al.*, "On the current research progress of metallic materials fabricated by laser powder bed fusion process: a review," *Journal of Materials Research and Technology,* vol. 20, pp. 681-707, 2022, doi: 10.1016/j.jmrt.2022.07.085.
[99] W. M. Steen, and Jyotirmoy Mazumder., "Laser material processing.," *springer science & business media,* 2010.
[100] A. W. D. Biswajit Basu, "Rapid solidification following laser melting of pure metals—I. Study of flow field and role of convection," *International Journal of Heat and Mass Transfer,* vol. 35, no. 5, pp. 1049-1058, 1992, doi: https://doi.org/10.1016/0017-9310(92)90165-O.
[101] A. W. D. Biswajit Basu, "Rapid solidification following laser melting of pure metals—II. Study of pool and solidification characteristics," *International Journal of Heat and Mass Transfer,* vol. 35, no. 5, pp. 1059-1067, 1992, doi: https://doi.org/10.1016/0017-9310(92)90166-P.
[102] A. B. G. M.H. Loretto, D. Hu, P.A. Blenkinsop, I.P. Jones, T.T. Cheng,, "The influence of composition and processing on the structure and properties of TiAl-based alloys," *Intermetallics,* vol. 6, no. 7 - 8, 1998, doi: https://doi.org/10.1016/S0966-9795(98)00035-1.
[103] A. Charmi *et al.*, "Mechanical anisotropy of additively manufactured stainless steel 316L: An experimental and numerical study," *Materials Science and Engineering: A,* vol. 799, 2021, doi: 10.1016/j.msea.2020.140154.
[104] R. F. A. Charmi, L. Ávila, G. Mohr, K. Sommer, A. Ulbricht, M. Sprengel, R. Saliwan Neumann, B. Skrotzki, A. Evans,, "Mechanical anisotropy of additively manufactured stainless steel 316L: An experimental and numerical study," *Materials Science and Engineering,* vol. 799, 2021, doi: https://doi.org/10.1016/j.msea.2020.140154.

[105] C. C. R. Xueyang Li, Thomas Tancogne-Dejean, Dirk Mohr, "Rate- and temperature-dependent plasticity of additively manufactured stainless steel 316L: Characterization, modeling and application to crushing of shell-lattices," *International Journal of Impact Engineering,* vol. 145, 2020, doi: https://doi.org/10.1016/j.ijimpeng.2020.103671.

[106] X. G. Wei Jiang, Yunlai Deng,, "Anisotropic response in mechanical behavior of additively manufactured Al–Mn-Sc alloys by in-situ EBSD tensile tests," *Materials Science and Engineering,* vol. 858, 2022, doi: https://doi.org/10.1016/j.msea.2022.144155.

[107] B. Z. Raiyan Seede, Austin Whitt, Sezer Picak, Sean Gibbons, Philip Flater, Alaa Elwany, Raymundo Arroyave, Ibrahim Karaman,, "Effect of heat treatments on the microstructure and mechanical properties of an ultra-high strength martensitic steel fabricated via laser powder bed fusion additive manufacturing,," *Additive Manufacturing,* vol. 47, 2021, doi: https://doi.org/10.1016/j.addma.2021.102255.

[108] F. M. F. Fathin Iliana Jamhari, Minhalina Ahmad Buhairi, Abu Bakar Sulong, Nabilah Afiqah Mohd Radzuan, Norhamidi Muhamad, Intan Fadhlina Mohamed, Nashrah Hani Jamadon, Kim Seah Tan,, "Influence of heat treatment parameters on microstructure and mechanical performance of titanium alloy in LPBF: A brief review," *Journal of Materials Research and Technology,* vol. 24, 2023, doi: https://doi.org/10.1016/j.jmrt.2023.04.090.

[109] A. Evangelou *et al.*, "Effects of process parameters and scan strategy on the microstructure and density of stainless steel 316 L produced via laser powder bed fusion," *Journal of Alloys and Metallurgical Systems,* vol. 3, 2023, doi: 10.1016/j.jalmes.2023.100027.

[110] C. Zhou, F. Wu, D. Tang, Z. Zhang, L. Zhang, and J. Zheng, "Effect of subcritical-temperature heat treatment on corrosion of SLM SS316L with different process parameters," *Corrosion Science,* vol. 218, 2023, doi: 10.1016/j.corsci.2023.111214.

[111] N. Wawrzyniak, P. R. Provencher, M. Brochu, and M. Brochu, "Tensile properties of SS316L produced by LPBF: Influence of specimen dimensions and surface condition," *Materials Characterization,* vol. 203, 2023, doi: 10.1016/j.matchar.2023.113117.

[112] Z. Sun, X. Tan, S. B. Tor, and W. Y. Yeong, "Selective laser melting of stainless steel 316L with low porosity and high build rates," *Materials & Design,* vol. 104, pp. 197-204, 2016, doi: 10.1016/j.matdes.2016.05.035.

[113] Y. Zhong, L. Liu, S. Wikman, D. Cui, and Z. Shen, "Intragranular cellular segregation network structure strengthening 316L stainless steel prepared by selective laser melting," *Journal of Nuclear Materials,* vol. 470, pp. 170-178, 2016, doi: 10.1016/j.jnucmat.2015.12.034.

[114] D. Wang, C. Song, Y. Yang, and Y. Bai, "Investigation of crystal growth mechanism during selective laser melting and mechanical property characterization of 316L stainless steel parts," *Materials & Design,* vol. 100, pp. 291-299, 2016, doi: 10.1016/j.matdes.2016.03.111.

[115] A. Ghosh, S. Biswas, T. Turner, A.-M. Kietzig, and M. Brochu, "Surface, microstructure, and tensile deformation characterization of LPBF SS316L microstruts micromachined with femtosecond laser," *Materials & Design,* vol. 210, 2021, doi: 10.1016/j.matdes.2021.110045.

[116] C. Wang, P. Zhu, Y. H. Lu, and T. Shoji, "Effect of heat treatment temperature on microstructure and tensile properties of austenitic stainless 316L using wire and arc additive manufacturing," *Materials Science and Engineering: A,* vol. 832, 2022, doi: 10.1016/j.msea.2021.142446.

[117] E. W. Hovig, A. S. Azar, F. Grytten, K. Sørby, and E. Andreassen, "Determination of Anisotropic Mechanical Properties for Materials Processed by Laser Powder Bed Fusion," *Advances in Materials Science and Engineering,* vol. 2018, pp. 1-20, 2018, doi: 10.1155/2018/7650303.

[118] Z. Pitrmuc *et al.*, "Mechanical and Microstructural Anisotropy of Laser Powder Bed Fusion 316L Stainless Steel," *Materials (Basel),* vol. 15, no. 2, Jan 12 2022, doi: 10.3390/ma15020551.

[119] K. Benarji, Y. Ravi Kumar, A. N. Jinoop, C. P. Paul, and K. S. Bindra, "Effect of Heat-Treatment on the Microstructure, Mechanical Properties and Corrosion Behaviour of SS 316 Structures Built by Laser Directed Energy Deposition Based Additive Manufacturing," *Metals and Materials International,* vol. 27, no. 3, pp. 488-499, 2020, doi: 10.1007/s12540-020-00838-y.
[120] P. Krakhmalev *et al.*, "Microstructure, Solidification Texture, and Thermal Stability of 316 L Stainless Steel Manufactured by Laser Powder Bed Fusion," *Metals,* vol. 8, no. 8, 2018, doi: 10.3390/met8080643.
[121] O. O. Salman, C. Gammer, A. K. Chaubey, J. Eckert, and S. Scudino, "Effect of heat treatment on microstructure and mechanical properties of 316L steel synthesized by selective laser melting," *Materials Science and Engineering: A,* vol. 748, pp. 205-212, 2019, doi: 10.1016/j.msea.2019.01.110.
[122] P. Deng *et al.*, "On the Thermal Stability of Dislocation Cellular Structures in Additively Manufactured Austenitic Stainless Steels: Roles of Heavy Element Segregation and Stacking Fault Energy," *Jom,* vol. 72, no. 12, pp. 4232-4243, 2020, doi: 10.1007/s11837-020-04427-7.
[123] T. Voisin *et al.*, "New insights on cellular structures strengthening mechanisms and thermal stability of an austenitic stainless steel fabricated by laser powder-bed-fusion," *Acta Materialia,* vol. 203, 2021, doi: 10.1016/j.actamat.2020.11.018.
[124] J. Bedmar, S. García-Rodríguez, M. Roldán, B. Torres, and J. Rams, "Effects of the heat treatment on the microstructure and corrosion behavior of 316 L stainless steel manufactured by Laser Powder Bed Fusion," *Corrosion Science,* vol. 209, 2022, doi: 10.1016/j.corsci.2022.110777.
[125] F. Bosio *et al.*, "A time-saving and cost-effective method to process alloys by Laser Powder Bed Fusion," *Materials & Design,* vol. 181, 2019, doi: 10.1016/j.matdes.2019.107949.
[126] S. Vock, B. Klöden, A. Kirchner, T. Weißgärber, and B. Kieback, "Powders for powder bed fusion: a review," *Progress in Additive Manufacturing,* vol. 4, no. 4, pp. 383-397, 2019, doi: 10.1007/s40964-019-00078-6.
[127] R. O. C. a. D. B. N E Gorji, "XPS, XRD, and SEM characterization of the virgin and recycled metallic powders for 3D printing applications," presented at the IOP Conference Series: Materials Science and Engineering.
[128] V. V. Popov *et al.*, "Powder Bed Fusion Additive Manufacturing Using Critical Raw Materials: A Review," *Materials (Basel),* vol. 14, no. 4, Feb 14 2021, doi: 10.3390/ma14040909.
[129] S. F. Mélanie Despeisse, "The Role of Additive Manufacturing in Improving

Resource Efficiency and Sustainability," presented at the Conference: IFIP International Conference on Advances in Production Management Systems, 2015.
[130] E. Santecchia, S. Spigarelli, and M. Cabibbo, "Material Reuse in Laser Powder Bed Fusion: Side Effects of the Laser—Metal Powder Interaction," *Metals,* vol. 10, no. 3, 2020, doi: 10.3390/met10030341.
[131] J. A. Slotwinski, E. J. Garboczi, P. E. Stutzman, C. F. Ferraris, S. S. Watson, and M. A. Peltz, "Characterization of Metal Powders Used for Additive Manufacturing," *J Res Natl Inst Stand Technol,* vol. 119, pp. 460-93, 2014, doi: 10.6028/jres.119.018.
[132] T. P. B. Sartin , B. Griffith , W. Everhart , L. Elder , E. Wenski , C. Cook , and W. K. D. Wieliczka , A. Rubenchik , S. Wu , B. Brown , C. Johnson , J. Crow, "316L Powder Reuse for Metal Additive Manufacturing," *University of Texas at Austin,* 2017. [Online]. Available: https://hdl.handle.net/2152/89828.
[133] L. C. Ardila *et al.*, "Effect of IN718 Recycled Powder Reuse on Properties of Parts Manufactured by Means of Selective Laser Melting," *Physics Procedia,* vol. 56, pp. 99-107, 2014, doi: 10.1016/j.phpro.2014.08.152.

[134] D. Wang, Y. Yang, Z. Yi, and X. Su, "Research on the fabricating quality optimization of the overhanging surface in SLM process," *The International Journal of Advanced Manufacturing Technology,* vol. 65, no. 9-12, pp. 1471-1484, 2012, doi: 10.1007/s00170-012-4271-4.
[135] B. B. Ravichander *et al.*, "Cost-Aware Design and Fabrication of New Support Structures in Laser Powder Bed Fusion: Microstructure and Metallurgical Properties," *Applied Sciences,* vol. 11, no. 21, 2021, doi: 10.3390/app112110127.
[136] G. Strano, L. Hao, R. M. Everson, and K. E. Evans, "A new approach to the design and optimisation of support structures in additive manufacturing," *The International Journal of Advanced Manufacturing Technology,* vol. 66, no. 9-12, pp. 1247-1254, 2013, doi: 10.1007/s00170-012-4403-x.
[137] R. Vaidya and S. Anand, "Optimum Support Structure Generation for Additive Manufacturing Using Unit Cell Structures and Support Removal Constraint," *Procedia Manufacturing,* vol. 5, pp. 1043-1059, 2016, doi: 10.1016/j.promfg.2016.08.072.
[138] M. X. Gan and C. H. Wong, "Practical support structures for selective laser melting," *Journal of Materials Processing Technology,* vol. 238, pp. 474-484, 2016, doi: 10.1016/j.jmatprotec.2016.08.006.
[139] A. Hussein, L. Hao, C. Yan, R. Everson, and P. Young, "Advanced lattice support structures for metal additive manufacturing," *Journal of Materials Processing Technology,* vol. 213, no. 7, pp. 1019-1026, 2013, doi: 10.1016/j.jmatprotec.2013.01.020.
[140] F. Calignano, "Design optimization of supports for overhanging structures in aluminum and titanium alloys by selective laser melting," *Materials & Design,* vol. 64, pp. 203-213, 2014, doi: 10.1016/j.matdes.2014.07.043.
[141] T. Mishurova *et al.*, "The Influence of the Support Structure on Residual Stress and Distortion in SLM Inconel 718 Parts," *Metallurgical and Materials Transactions A,* vol. 49, no. 7, pp. 3038-3046, 2018, doi: 10.1007/s11661-018-4653-9.
[142] Y. Kajima *et al.*, "Effect of adding support structures for overhanging part on fatigue strength in selective laser melting," *J Mech Behav Biomed Mater,* vol. 78, pp. 1-9, Feb 2018, doi: 10.1016/j.jmbbm.2017.11.009.
[143] H. Chen, D. Gu, J. Xiong, and M. Xia, "Improving additive manufacturing processability of hard-to-process overhanging structure by selective laser melting," *Journal of Materials Processing Technology,* vol. 250, pp. 99-108, 2017, doi: 10.1016/j.jmatprotec.2017.06.044.
[144] Y. Liu, Y. Yang, and D. Wang, "A study on the residual stress during selective laser melting (SLM) of metallic powder," *The International Journal of Advanced Manufacturing Technology,* vol. 87, no. 1-4, pp. 647-656, 2016, doi: 10.1007/s00170-016-8466-y.
[145] F. C. Pinto, I. R. Souza Filho, M. J. R. Sandim, and H. R. Z. Sandim, "Defects in parts manufactured by selective laser melting caused by δ-ferrite in reused 316L steel powder feedstock," *Additive Manufacturing,* vol. 31, 2020, doi: 10.1016/j.addma.2019.100979.
[146] S. Pal, G. Lojen, V. Kokol, and I. Drstvenšek, "Reducing porosity at the starting layers above supporting bars of the parts made by Selective Laser Melting," *Powder Technology,* vol. 355, pp. 268-277, 2019, doi: 10.1016/j.powtec.2019.07.059.
[147] S. R. Trisnanto, X. Wang, M. Brochu, and S. Omanovic, "Effects of crystallographic orientation on the corrosion behavior of stainless steel 316L manufactured by laser powder bed fusion," *Corrosion Science,* vol. 196, 2022, doi: 10.1016/j.corsci.2021.110009.
[148] Y. M. Wang *et al.*, "Additively manufactured hierarchical stainless steels with high strength and ductility," *Nature Materials,* vol. 17, no. 1, pp. 63-71, 2017, doi: 10.1038/nmat5021.

[149] M. Shamsujjoha, S. R. Agnew, J. M. Fitz-Gerald, W. R. Moore, and T. A. Newman, "High Strength and Ductility of Additively Manufactured 316L Stainless Steel Explained," *Metallurgical and Materials Transactions A,* vol. 49, no. 7, pp. 3011-3027, 2018, doi: 10.1007/s11661-018-4607-2.
[150] K. Saeidi, X. Gao, Y. Zhong, and Z. J. Shen, "Hardened austenite steel with columnar sub-grain structure formed by laser melting," *Materials Science and Engineering: A,* vol. 625, pp. 221-229, 2015, doi: 10.1016/j.msea.2014.12.018.
[151] D. Guo *et al.*, "Solidification microstructure and residual stress correlations in direct energy deposited type 316L stainless steel," *Materials & Design,* vol. 207, 2021, doi: 10.1016/j.matdes.2021.109782.
[152] T. Mukherjee, H. L. Wei, A. De, and T. DebRoy, "Heat and fluid flow in additive manufacturing – Part II: Powder bed fusion of stainless steel, and titanium, nickel and aluminum base alloys," *Computational Materials Science,* vol. 150, pp. 369-380, 2018, doi: 10.1016/j.commatsci.2018.04.027.
[153] M. A. Chaudry, G. Mohr, and K. Hilgenberg, "Experimental and numerical comparison of heat accumulation during laser powder bed fusion of 316L stainless steel," *Progress in Additive Manufacturing,* vol. 7, no. 5, pp. 1071-1083, 2022, doi: 10.1007/s40964-022-00282-x.
[154] Z. Luo and Y. Zhao, "Numerical simulation of part-level temperature fields during selective laser melting of stainless steel 316L," *The International Journal of Advanced Manufacturing Technology,* vol. 104, no. 5-8, pp. 1615-1635, 2019, doi: 10.1007/s00170-019-03947-0.
[155] M. J. AZIZ and T. KAPLAN, "CONTINUOUS GROWTH MODEL FOR INTERFACE MOTION DURING ALLOY SOLIDIFICATION," *Acta metall.,* vol. 36, no. 8, pp. 2335-2347, 1988, doi: https://doi.org/10.1016/0001-6160(88)90333-1.
[156] C. Qiu, M. A. Kindi, A. S. Aladawi, and I. A. Hatmi, "A comprehensive study on microstructure and tensile behaviour of a selectively laser melted stainless steel," *Sci Rep,* vol. 8, no. 1, p. 7785, May 17 2018, doi: 10.1038/s41598-018-26136-7.
[157] Y. Miyata, M. Okugawa, Y. Koizumi, and T. Nakano, "Inverse Columnar-Equiaxed Transition (CET) in 304 and 316L Stainless Steels Melt by Electron Beam for Additive Manufacturing (AM)," *Crystals,* vol. 11, no. 8, 2021, doi: 10.3390/cryst11080856.
[158] R. C. Chen, C. Hong, J. J. Li, Z. Z. Zheng, and P. C. Li, "Austenite grain growth and grain size distribution in isothermal heat-treatment of 300M steel," *Procedia Engineering,* vol. 207, pp. 663-668, 2017, doi: 10.1016/j.proeng.2017.10.1038.
[159] T. Dudziak *et al.*, "Effect of 316L Stainless Steel Fabrication on Oxidation Resistance, Surface Morphology, and Hot Tensile Behavior," *Journal of Materials Engineering and Performance,* 2023, doi: 10.1007/s11665-023-08321-6.
[160] M. Taylor and J. Husband, "Oxidation of SS304 and SS316 and the formation of diffusionally isolated regions leading to localised premature breakaway oxidation," *Materials at High Temperatures,* vol. 40, no. 4, pp. 318-330, 2023, doi: 10.1080/09603409.2023.2177938.
[161] J. Wendel, S. K. Manchili, E. Hryha, and L. Nyborg, "Reduction of surface oxide layers on water-atomized iron and steel powder in hydrogen: Effect of alloying elements and initial powder state," *Thermochimica Acta,* vol. 692, 2020, doi: 10.1016/j.tca.2020.178731.
[162] G. H. Kwon, H. Park, B. Choi, Y. K. Lee, and K. Moon, "Influence of Cr Content on the High-Temperature Oxidation Behavior and Mechanism of Low-Alloy Steels," *Materials (Basel),* vol. 16, no. 14, Jul 12 2023, doi: 10.3390/ma16144964.
[163] H. J. T. Ellingham, "Reducibility of oxides and sulfides in metallurgical processes," *Journal of the Society of Chemical Industry,* vol. 63, pp. 125-160, 1944.

[164] R. E. Lobnig, H. P. Schmidt, K. Hennesen, and H. J. Grabke, "Diffusion of cations in chromia layers grown on iron-base alloys," *Oxidation of Metals,* vol. 37, no. 1-2, pp. 81-93, 1992, doi: 10.1007/bf00665632.

[165] F. B. Riffard, H. ; Caudron, E. ; Cueff, R. ; Rabaste, F. ; Issartel, C., "In situ and glancing angle X-ray diffraction of the structure change during and after the high temperature oxidation at 1000 “C in air of an yttrium-implanted 304 steel " *Journal de Physique IV (Proceedings),* vol. 12, no. 6, pp. 265-272, 2002, doi: 10.1051/jp4:20020235.

[166] R. K. WILD, "HIGH TEMPERATURE OXIDATION OF AUSTENITIC STAINLESS STEEL IN LOW OXYGEN PRESSURE," *Corrosion Science,* vol. 17, pp. 87-104, 1977, doi: https://doi.org/10.1016/0010-938X(77)90011-7.

[167] A. C. S. Sabioni, A. M. Huntz, L. C. Borges, and F. Jomard, "First study of manganese diffusion in Cr2O3polycrystals and thin films by SIMS," *Philosophical Magazine,* vol. 87, no. 12, pp. 1921-1937, 2007, doi: 10.1080/14786430601120462.

[168] X. Wang, L. N. Carter, B. Pang, M. M. Attallah, and M. H. Loretto, "Microstructure and yield strength of SLM-fabricated CM247LC Ni-Superalloy," *Acta Materialia,* vol. 128, pp. 87-95, 2017, doi: 10.1016/j.actamat.2017.02.007.

[169] N. Karimi *et al.*, "Characterization of the oxides formed at 1000°C on the AISI 304 stainless steel by X-ray diffraction and infrared spectroscopy," *Applied Surface Science,* vol. 254, no. 8, pp. 2292-2299, 2008, doi: 10.1016/j.apsusc.2007.09.018.

[170] R. C. Lobb, J. A. Sasse, and H. E. Evans, "Dependence of oxidation behaviour on silicon content of 20%Cr austenitic steels," *Materials Science and Technology,* vol. 5, no. 8, pp. 828-834, 2013, doi: 10.1179/mst.1989.5.8.828.

[171] R. Bauer, M. Baccalaro, L. P. H. Jeurgens, M. Pohl, and E. J. Mittemeijer, "Oxidation Behavior of Fe–25Cr–20Ni–2.8Si During Isothermal Oxidation at 1,286 K; Life-time Prediction," *Oxidation of Metals,* vol. 69, no. 3-4, pp. 265-285, 2008, doi: 10.1007/s11085-008-9097-y.

[172] M. J. Bennett, J. A. Desport, and P. A. Labun, "Transverse microstructure of an oxide scale formed on a 20% Cr–25% Ni–niobium stabilized stainless steel," *Proceedings of the Royal Society of London. A. Mathematical and Physical Sciences,* vol. 412, no. 1842, pp. 223-230, 1987, doi: 10.1098/rspa.1987.0086.

[173] H. E. Evans, D. A. Hilton, R. A. Holm, and S. J. Webster, "Influence of silicon additions on the oxidation resistance of a stainless steel," *Oxidation of Metals,* vol. 19, no. 1-2, pp. 1-18, 1983, doi: 10.1007/bf00656225.

[174] M. J. Bennett, J. A. Desport, and P. A. Labun, "Analytical electron microscopy of a selective oxide scale formed on 20% Cr-25% Ni-Nb stainless steel," *Oxidation of Metals,* vol. 22, no. 5-6, pp. 291-306, 1984, doi: 10.1007/bf00656580.

[175] H. Fujikawa and Y. Iijima, "Effect of Grain Size on the High Temperature Oxidation Behaviour of Austenitic Stainless Steels," *Defect and Diffusion Forum,* vol. 333, pp. 149-155, 2013, doi: 10.4028/www.scientific.net/DDF.333.149.

[176] S. Samal and S. K. Mitra, "Influence of Grain Shape, Size, and Grain Boundary Diffusion on High-Temperature Oxidation of Pure Metal Fe, Cu, and Zn," *Metallurgical and Materials Transactions A,* vol. 46, no. 8, pp. 3324-3332, 2015, doi: 10.1007/s11661-015-2987-0.

[177] V. B. Trindade, U. Krupp, P. E. G. Wagenhuber, and H. J. Christ, "Oxidation mechanisms of Cr-containing steels and Ni-base alloys at high-temperatures –. Part I: The different role of alloy grain boundaries," *Materials and Corrosion,* vol. 56, no. 11, pp. 785-790, 2005, doi: 10.1002/maco.200503879.